Mature and migratory dendritic cells promote immune infiltration and response to anti-PD-1 checkpoint blockade in metastatic melanoma

Jiekun Yang[1,2,3,4*†], Cassia Wang[1*], Doris Fu[1*], Li-Lun Ho[1,2], Kyriakitsa Galani[1,2], Lee Chen[1], Dennie T Frederick[5], Liang He[1,2], Amy Y. Huang[2,6,7], Emily J. Robitschek[2,6,7], Sandeep K. Yadav[8], Wentao Deng[8], Rahul Tacke[1], Kelly P. Burke[2,6,7], Tatyana Sharova[9], Kunal Rai[8], David Liu[2,6,7], Genevieve M. Boland[2,9†], Manolis Kellis[1,2†]

[1] Computer Science and Artificial Intelligence Laboratory, Massachusetts Institute of Technology, Cambridge, MA, USA. [2] Broad Institute of MIT and Harvard, Cambridge, MA, USA. [3] Department of Genetics, School of Arts and Sciences, Rutgers University-New Brunswick, Piscataway, NJ, USA. [4] Human Genetics Institute of New Jersey, Rutgers University-New Brunswick, Piscataway, NJ, USA. [5] Division of Medical Oncology, Department of Medicine, Massachusetts General Hospital Cancer Center, Harvard Medical School, Boston, MA, USA. [6] Dana-Farber Cancer Institute, Boston, MA, USA. [7] Harvard Medical School, Boston, MA, USA. [8] Department of Genomic Medicine and MDACC Epigenomics Therapy Initiative, University of Texas MD Anderson Cancer Center, Houston, TX, USA. [9] Division of Gastrointestinal and Oncologic Surgery, Department of Surgery, Massachusetts General Hospital Cancer Center, Harvard Medical School, Boston, MA, USA. * Equal contributors. † Correspondence to: jackie.yang@rutgers.edu, GMBOLAND@MGH.HARVARD.EDU, manoli@mit.edu

Abstract

Immune checkpoint inhibitors (ICIs) have heralded a remarkable shift in cancer care, significantly extending survival for advanced cancer patients. However, despite their remarkable clinical successes, a substantial majority of patients fail to achieve a lasting response to ICIs. To address this challenge and gain insights into the complex landscape of the tumor microenvironment (TME), we conducted an extensive analysis using single-cell RNA sequencing (scRNA; ~216K cells across 39 samples) and single-nucleus transposase-accessible chromatin sequencing (snATAC; ~43K cells from 15 samples) in a metastatic melanoma cohort. This systematic approach delineates 14 distinct cell types and 55 cell subtypes, including the identification of 15 transcriptional hallmarks of malignant cells. Through correlation analysis of cell subtype proportions, we unveiled six distinct clusters associated with varying tumor responses. Particularly intriguing was the identification of the mature DC enriched in immunoregulatory molecules (mregDC) subtype exhibiting correlations with naive T and B cells, forming an anti-tumor program that underscores the importance of multiple immune cell types in mediating anti-tumor immunity. Notably, we found that mregDC abundance represents a good prognostic predictor of progression-free survival (PFS) in the context of ICI treatment, and when combined with the TCF7+/- CD8 T cell ratio, it reliably predicts patient PFS across treatments beyond ICI. We validated our findings using an independent cohort of 274 ICI-treated melanoma samples analyzed using tissue-level expression. We next compared mregDCs and conventional dendritic cell types 1 and 2 (cDC1 and cDC2) using transcriptome signature, differentiation trajectory, interactome, cytokine milieu, and epigenome landscape analyses. This comparative analysis shed light on the unique attributes of mregDCs within the TME. Finally, we investigated cell type/subtype-specific genes, pathways, immune response enrichment, and ligand-receptor interactions closely associated with the proportions of mregDCs within the TME. These molecular and cellular insights, with their critical roles in enhancing the immune response against cancer, offer valuable prospects for predicting the efficacy of ICI regimens, and potentially guiding the selection of rational combinatorial therapies.

Introduction

Cancer treatment has progressed significantly, moving beyond targeting highly proliferative cells to identifying precise targets within cancer cells and their specific immune microenvironment. Combination therapies, whether administered simultaneously or sequentially, are frequently used for increased efficacy in advanced cancer stages. The emergence of immune checkpoint inhibitors (ICIs) approximately a decade ago and their use in advanced melanoma revolutionized cancer treatment[1]. Prior to ICIs, patients with stage IV melanoma typically had a median lifespan of 6-9 months. However, with ICIs, survival rates extended up to 6 years with anti-PD-1/anti-CTLA-4 combination therapy, albeit with a higher incidence of severe adverse events[2]. Despite these advancements, only a subset of patients, ranging from 45 to 58%, demonstrated objective responses to individual or combined ICI treatments[3]. ICI treatments, used as a second-line treatment option, showed objective responses in only 15 to 30% of patients[4]. Resistance to targeted therapies and ICIs has posed

challenges to patients' progression-free survival (PFS), underscoring the urgent need for biomarkers to predict survival benefits across treatments and guide clinical decision-making.

Over the past decade, research in metastatic melanoma has identified several response-associated biological features, such as tumor mutational burden (TMB) and neoantigen load[5], alongside CD8 expression at the invasive margin[6]. However, their predictive abilities remain limited. Advancements in single-cell technology have facilitated a more nuanced understanding of the tumor microenvironment (TME) at single-cell resolution and its relationship with clinical responses. Initially, Tirosh *et al*.[7] employed single-cell RNA sequencing (scRNA-seq) to analyze 4,645 single cells from 19 metastatic melanoma patients, revealing the multicellular ecosystem of tumors. Subsequently, Jerby-Arnon *et al.*[8] combined 2,987 scRNA-seq profiled cells from 17 newly collected patient tumors with 4,199 cells from Tirosh *et al*.[7], identifying a resistance program expressed by malignant cells, CDK4/6 signaling, linked to T cell exclusion and immune evasion. In parallel, Sade-Feldman *et al*.[9] profiled transcriptomes of 16,291 individual immune cells from 48 tumor samples of melanoma patients treated with ICIs, establishing a TCF7+/- CD8 T cell ratio associated with response to ICIs. More recently, Zhang *et al*.[10] performed scRNA-seq on 63,694 cells from 5 acral and 3 cutaneous melanoma samples, comparing immune differences between the two melanoma subtypes. However, these studies have primarily focused on tumor and immune cells, particularly T cells, due to limitations in cell collection and technology costs.

Dendritic cells (DCs) play a crucial role in coordinating immune responses against tumors, serving as professional antigen-presenting cells (APCs) since their discovery in 1973[11]. Categorized into conventional DCs (cDCs) and plasmacytoid DCs (pDCs), cDCs further split into type 1 (cDC1) and type 2 (cDC2) based on lineage-determining TFs and functions[12–14]. While immature cDCs are essential for immune surveillance, their maturation is vital for immunogenicity involving antigen processing, presentation, and T-cell co-stimulation[15]. Despite their importance, DC signatures has been obscured in tumor measurements due to its low abundance[11], until recent single-cell sequencing efforts unveiled their heterogeneity, highlighting a regulatory signature termed mature DC enriched in immunoregulatory molecules (mregDCs)[16]. Although prior studies associated a higher density of mregDC-like dendritic cells with improved survival in cutaneous melanoma[17], this state remains poorly characterized in melanoma across different treatments.

To address these gaps, we conducted extensive single-cell profiling of metastatic melanoma samples, annotating diverse cell types and subtypes in the TME and correlating them with treatment response and patient survival. Analyzing 215,946 cells across 39 samples, we identified 14 cell types and 55 subtypes, shedding light on correlated subtypes and prognostic markers beyond immune checkpoint inhibitors (ICIs). Of particular interest were mregDCs, which emerged as survival predictors. We delved into their transcriptome signatures, epigenome landscape, differentiation trajectory, and cell-cell communication potentials, uncovering intrinsic and extrinsic molecules associated with mregDC abundance.

Results

Cell types in metastatic melanoma tumor microenvironment

We obtained metastatic melanoma samples from Massachusetts General Hospital, focusing on annotated cases that had received various primary treatments, predominantly involving ICIs. After rigorous quality control, our analysis centered on 39 scRNA-seq samples, complemented by 15 paired snATAC-seq samples. Out of the 39 scRNA-seq samples, 31 underwent treatment that included ICI therapy, with 19 of them exclusively receiving ICI treatment. Key clinical information, such as progression-free survival (PFS), overall survival (OS), lesional response, treatment details, tissue type, melanoma subtype, sex, age, and time relative to treatment initiation, is visualized in **Figure 1A** and listed in **Supplementary Table 1**.

We conducted data integration for the 39 scRNA-seq samples, implemented dimensionality reduction techniques, and illustrated the 2D cell embeddings. At the highest level, we distinguished tumor, immune, and stromal compartments, along with sample IDs, tissues, melanoma subtypes, sex, treatment groups, treatment state, and lesional responses (**Extended Data Fig. 1, Fig. 1B**). We identified 14 cell types for the 215,946 cells, including sample-specific tumor cells (further analyzed in the subsequent section), T lymphocytes (i.e., CD8 T cells, CD4 T cells, other T cells, and cycling T cells), natural killer (NK) cells, B lymphocytes, myeloid cells (encompassing monocytes/macrophages, conventional dendritic cells [cDC], plasmacytoid dendritic cells [pDC], and mast cells), and stromal cells (including endothelial cells, fibroblasts, and keratinocytes; **Fig. 1B**). Distinct expression patterns of canonical cell type-specific markers are presented in **Figure 1C**.

Our single-cell annotations showed highly consistent cell type annotations with previous studies on metastatic melanoma, and contributed more cells than all previous studies combined (**Supplementary Fig. 1A-D**)[7–10]. We also confirmed that our cell type markers and cell type annotations remained consistent when jointly analyzing our data with cells from all previous studies combined (**Supplementary Fig. 1E**).

Consensus tumor programs and immune cell subtypes in tumor microenvironment

We found that transcriptomic profiles of tumor cells exhibit patient-specific patterns (**Extended Data Fig. 1B**), as found in previous studies[18]. To correct for these patient specific effects and identify tumor-shared patterns of intra-tumor heterogeneity (ITH), we assigned tumor cells to 15 distinct meta-programs previously compiled in Gavish et al.[18] encompassing 30,162 high-quality cells with a minimum number of 25 expressed genes in the meta-program (**Fig. 2A**, **Extended Data Fig. 2A**). The predominant gene expression patterns in each meta-program provide insights into the unique functionalities of different tumor cell subpopulations within a tumor. These functionalities span various aspects, including cell-cycle phases (G1/S, G2/M, HMG-rich), upregulation of processes such as epithelial-mesenchymal transition (EMT), hypoxia, interferon and major histocompatibility complex (MHC) class II, MYC, protein maturation, respiration, skin pigmentation, stress, translation initiation, and unfolded protein response (**Fig. 2B**). Our analysis confirms previously-reported meta-programs[18] and also facilitates correlation of these tumor programs with non-tumor subtypes within the same samples.

For myeloid cells, we classified monocytes into classical ($CD14^+FCN1^+S100A8^+S100A9^+$) and non-classical ($CD16^+LST1^+LILRB2^+$) monocytes; macrophages into M1, M2 and tumor-associated macrophages (TAMs); and cDCs into cDC type 1 (cDC1), type 2 (cDC2) and a mature and migratory subtype (mregDC; **Fig. 2C**, **Extended Data Fig. 2B**). We found that M1 macrophages, which participate in pro-inflammatory responses, are distinguished by their expression of CXCL9, CXCL10, CD80, FCGR1A, and HLA-DR. In contrast, M2 macrophages, known for their immunosuppressive role, exhibited expression of anti-inflammatory molecules MSR1, CD163, MRC1, C1Q, SELENOP, and APOE. TAMs were characterized by their expression of VEGFA, IL-10, TNF, and TGFB1. Further details about the cDC subtypes will be discussed in a subsequent section.

In the CD8+ T cell compartment, we identified various subtypes, including naive T cells (Tn, $CCR7^+$), effector T cells (Teff, $GZMA^+GZMB^+$), memory T cells (Tm, $CXCR6^+$), exhausted T cells (Tex), and natural killer T cells (NKT, $CD8^+XCL2^+$; **Fig. 2D** and **Extended Data Fig. 2C**). Among the Teff subset, three clusters exhibited moderate to high expression of cytotoxic markers GZMA and GZMB. An early activated Teff subgroup was marked by CD69 expression. Notably, HNRNPH1+ Teff displayed elevated levels of long non-coding RNAs (lncRNA) including MALAT1, NEAT1, and ribonucleoproteins HNRNPH1 and HNRNPU, implicated in regulating T-cell-mediated immune responses, potentially affecting ICI resistance[19]. Another distinct GZMK+ Teff cluster showed high expression of cytotoxicity-related genes, excluding CTLA-4. Within the Tm subset, cells were further categorized into effector memory T (Tem) and exhausted memory T (Texme) based on their expression of cytotoxic genes (GZMA, GZMB) and the exhaustion marker TOX. While checkpoint molecules like PDCD1, LAG3, TIGIT, and CTLA-4 were broadly expressed, detailed differential analysis revealed three distinct Tex cell clusters, each exhibiting distinct exhaustion and cytotoxicity profiles. Tex/HS displayed high expression of heat shock protein genes and enrichment in heat response-related pathways. The GNLY+ Tex cluster was unique for expressing granulysin gene GNLY and calcium-binding proteins S100A10 and S100A11. Additionally, the FTL+ Tex cluster exhibited increased expression of FTL and FTH1, encoding ferritin subunits. The role of ferritin in T cell function is still being explored, but prior studies have linked FTL and FTH1 to immune cell infiltration, particularly in Tregs[20].

We identified six subpopulations of $CD4^+$ T cells, including the commonly observed naive T cells (Tn), memory T cells (Tm), regulatory T cells (Tregs), exhausted T cells (Tex), $CD69^+$ early activated T cells ($CD69^+$ T), and NKT cells (**Fig. 2E**, **Extended Data Fig. 2D**). Notably, Tn cells, identified by their high expression of the naive marker CCR7, also exhibited significantly elevated expression of ribosomal genes, indicative of cells in a naive or quiescent state[21]. Tm cells expressed the memory marker CCL5. Tregs, governed by the transcription factor (TF) FOXP3, demonstrated elevated levels of co-inhibitory molecules CTLA-4 and TIGIT. Tex cells exhibited increased expression of checkpoint molecules, including TOX, CTLA-4, PDCD1, and TIGIT, along with an increase in glycolytic metabolism, highlighted by their elevated expression of GAPDH. The activated CD69+ T cell phenotype correlated with upregulation of stress-related genes, such as FOS, JUN, and heat shock protein (HSP) family genes. Additionally, we identified an NKT subpopulation characterized by its unique expression of XCL1, XCL2, KLRD1, and CD4, aligning with an innate lymphoid phenotype.

Furthermore, we uncovered a distinct subtype known as double negative NKT cells (DN NKT) among other T cells, characterized by the expression of T cell markers excluding CD4 and CD8, alongside NK markers. DN NKT cells have been proposed to adopt a pro-inflammatory phenotype, contributing to both innate and adaptive immunity[22]. For B cells, we categorized them into four subtypes: naive, transitional, memory, and plasma B cells. Naive B cells were marked by differentiating markers IGHD and IGHM, transitional B cells expressed CD93 and TNFRSF13C, memory B cells were identified by the presence of CD27, IGHM, IGHE, IGHG1, IGHA1, and IGHD, while (regulatory) plasma B cells expressed markers such as BCL6, IRF4, PRDM1, SDC1, TNFRSF17, and XBP1. In addition, we identified two subtypes of fibroblasts: myofibroblasts, expressing ACTA2, NDUFA4L2, and MYL9, and inflammatory fibroblasts, marked by the presence of IL6, CXCL12, and DPT.

In summary, our analysis revealed a total of 55 distinct cell subtypes within the 14 primary cell types in our cohort (**Extended Data Fig. 2E, Supplementary Table 2-4**). We later expanded these cell subtype annotations to the integrated single-cell atlas, encompassing data from five studies. This comprehensive subtyping offers an opportunity to explore correlations between these cell subtypes within the TME.

Cell subtype correlations reveal six modules with varied tumor responses

To analyze changes in subtype abundance dynamics within the TME, we calculated the relative proportions of cell subtypes in comparison to their respective cell types. Then we conducted correlations between these relative proportions across samples, resulting in the recognition of six distinct modules through unsupervised hierarchical clustering. We broadly categorized these modules using known functions of certain cell subtypes, specifically as having either anti-tumor, pro-tumor, or mixed characteristics (**Fig. 2F, Supplementary Table 5**).

In Module 1, correlations indicated a potential anti-tumor effect, with the mregDC subtype showing strong associations with CD8 Tn, CD8 HNRNPH1+ Teff, CD4 Tn, CD4 CD69+ T cells, CD4 NKT cells, and naive B cells. This module emphasized immune infiltration (**Extended Data Fig. 2F**). Module 2 exhibited pro-tumor characteristics, featuring correlations among CD8 FTL+ Tex cells, CD4 Treg cells, plasma B cells, and two tumor meta-programs (MYC and EMT). These associations suggested the suppression of immune functions. Module 3 presented mixed effects in terms of tumor response. For example, cDC1 was predominantly anti-tumor, while M2 macrophages tended to be pro-tumor[14]. In Module 4, correlations emerged among M1 macrophages, CD8 Tem cells, and tumor meta-programs related to unfolded protein response, stress, and interferon/MHC-II (**Extended Data Fig. 2G**). These cell subtypes were associated with anti-tumor responses, particularly through antigen presentation and inflammation. Module 5 included several exhausted T cell subtypes (e.g., CD4 Tex, CD8 Texme, CD8 Tex/HS, and CD8 GNLY+ Tex) and two pro-tumor myeloid cell subtypes, cDC2 and TAMs, showing a pro-tumor immune exhaustion signature (**Extended Data Fig. 2H**). Lastly, Module 6 pointed to an anti-tumor effector T cell function, with CD8 GZMK+ Teff, CD4 Tem cells, tumor meta-programs related to the cell cycle, and non-classical and classical monocytes (**Extended Data Fig. 2I**).

Upon focusing on the samples treated with ICI, we identified the same six modules as in **Fig. 2F**, albeit in a different order (**Supplementary Fig. 2A**), suggesting conserved cell subtype modules regardless of treatment. Expanding our correlation analysis to our integrated single-cell atlas with cell subtype annotations (**Supplementary Fig. 2B**), we still observed five of the six modules, although some module memberships were slightly altered or merged (**Supplementary Fig. 2C**). This variation can be attributed to the diverse cell types captured in each study due to different enrichment protocols. Notably, the anti-tumor immune infiltration module remained highly conserved, prompting us to explore its biological significance and its potential associations with clinical variables or responses.

Mature and migratory cDC abundance associated with ICI response and PFS

To identify cell subtypes with their abundance correlated with lesional response to treatment, we compared cell subtype relative proportions between respondering and non-responding tumors. Using all the samples, we observed more tumor cells with the stress meta-program, more Tregs, and more plasma B cells in non-responders ($p < 0.05$, **Extended Data Fig. 3A**). Tregs and plasma B cells belong to module 2 (pro-tumor immune suppression) in the above correlation analysis. We found more inflammatory fibroblasts ($p < 0.05$, **Extended Data Fig. 3A**), more tumor cells with the G2/M cell cycle program, and more CD8 Tn in responders ($p < 0.1$, **Supplementary Fig. 3A**). Tumor cells with the G2/M cell cycle program and CD8 Tn cells belong to two anti-tumor modules, modules 6 and 1, suggesting their anti-tumor effects across treatments. When focusing on the samples treated with only ICI (combo or anti-PD1), we detected more tumor cells with the

respiration tumor meta-program and M2 macrophages in non-responders, and more classical monocytes and mregDCs in responders (**Fig. 3A**). This finding highlights these cell types in mediating ICI-specific effects, and shows consistency with the known role of M2 macrophages and classical monocytes mediating anti- and pro-ICI effects, respectively[23]. mregDCs, transcriptionally characterized by single-cell studies[16,24,25], were reported to be more abundant in responsive triple-negative breast cancer patients during anti-PD-1 treatment[26], and they play an important role in mediating ICI effects in mouse models[27]. However, the underlying mechanism remains incompletely understood. Interestingly, neither cDC1 nor cDC2 was associated with treatment response in all the samples or subsets of samples (**Supplementary Fig. 3B**). mregDC did not show differential abundance in samples treated with therapies other than ICI only (**Supplementary Fig. 3C**). Relative proportions of cDC in all cells or all immune cells were not associated with treatment response (**Supplementary Fig. 3D**). In summary, these findings suggest that the relative proportion of cDCs showing the mature and regulatory phenotype could affect tumor's response to ICI.

Beyond treatment response, we observed significant PFS benefit and marginally significant OS benefit for ICI-treated samples with high relative proportions of mregDCs (**Fig. 3B**). Using the same median threshold to group samples into mregDC high versus low, we did not observe significant survival benefit for samples with other treatments, although mregDC high samples always showed higher survival probability compared to mregDC low samples (**Extended Fig. 3B,C**). None of the other cell subtypes associated with ICI response showed stratification of patient's survival; however, their survival curve splits were consistent with their corresponding effect directions for treatment response (**Supplementary Fig. 3E**). A previous single-cell metastatic melanoma study established an association between TCF7+ CD8 T cells and ICI response[9]. Here, we show that mregDC relative proportion is in fact particularly correlated with TCF7+ versus TCF7- CD8 T cell ratio (**Extended Data Fig. 3D**) and confirmed more TCF7+ CD8 T cells in responsive ICI-treated samples (**Extended Fig. 3E**). We also detected significant PFS and marginal OS benefit in ICI-treated samples with higher TCF7+ ratio (**Extended Fig. 3F**). Similar to mregDC relative proportion, TCF7 ratio did not stratify patient's survival in samples with other treatments (**Supplementary Fig. 3F**). However, when we combined these two potential biomarkers, they showed significant survival prediction power in all samples: samples with high mregDC proportion and high TCF7+ CD8 ratio had higher survival probability regardless of treatment type (**Fig. 3C**).

Moreover, we tested the derived mregDC signature (**Supplementary Table 3**) in a meta-metastatic melanoma cohort treated with ICI and with tissue-level RNA-seq data available[28]. We validated the association between mregDC signature scores and patient's response to ICI (n=274, **Fig. 3D**). The same mregDC signature score split by median showed significant PFS difference and marginal OS difference in this meta-cohort (**Fig. 3E**).

Transcriptional landscape of mature and migratory cDCs

We found that cDCs clustered into three subtypes: cDC1, cDC2 and mregDC (**Fig. 4A; Extended Fig. 4A**), and sought insights in their respective functions. cDC1 was characterized by high expression of canonical markers *CLEC9A* and *XCR1*, while cDC2 displayed elevated levels of *CD1C* and *FCER1A*. mregDC exhibited elevated expression of *LAMP3*, *FSCN1*, *CCL19*, and *CCR7*, consistent with prior findings[24,25]. Notably, cDC1 showed significant expression of its lineage-specific TF IRF8 among the three subtypes[29]. However, IRF4, the cDC2 lineage-specific TF, is expressed most prominently in mregDC compared to cDC1 and cDC2 (**Fig. 4B**). cDC1, cDC2 and mregDC scores based on previously reported signatures[16] confirmed our classification of the three subtypes (**Extended Fig. 4B**). The majority of published mregDC signatures are confirmed, with exceptions in Th2 response genes (**Supplementary Fig. 4A,B**)[16]. In contrast to mouse mregDCs, human mregDCs express higher levels of CCL22 and BCL2L1, while cDC2 exhibits higher levels of IL4I1, TNFRSF4, and STAT6 (**Supplementary Fig. 4B**).

Differential expression analysis revealed distinct gene expression profiles and pathways between mregDC and cDC1 as well as cDC2. Specifically, mregDC exhibited a higher number of up-regulated genes than down-regulated genes compared to cDC1 (611 vs. 85, **Fig. 4C, Supplementary Table 6**). The up-regulated genes were enriched in pathways involved in actin cytoskeleton organization, hydrolase activity, cell migration, NF-κB signaling, death receptor signaling, protein phosphorylation, cytokine signaling, T-cell costimulation and T-cell co-inhibition, aligning with the mature, activated, migratory and immunoregulatory features of mregDC (**Fig. 4D, Supplementary Table 7**). When comparing mregDC with cDC2, mregDC showed higher expression of 305 DEGs and lower expression of 419 genes (**Fig. 4E**). The up-regulated pathways predominantly related to T-cell activation with virus infection, TNFR1 signaling and kinase activity, whereas the down-regulated

pathways included immune response to bacterium (**Fig. 4F**). Based on the observed differences in pathways between mregDC and cDC1/cDC2, mregDC likely derives from cDC1, with gene programs associated with relevant phenotypes activated.

Upon comparing the expression patterns of select genes from a prior study[30], we noted that many markers previously associated with high expression in cDC1 populations were exclusively expressed by mregDCs in our cohort. These markers include CCR7 and CCL22 for migration, CD86, CD80, and CD40 for maturation, PDL2 and RANK for immunoregulation, and TAPBP for cross-presentation. This finding further strengthens the notion that cDC1 cells are a primary source of mregDCs in the human TME (**Supplementary Fig. 4C**). Additionally, there are markers equally expressed by cDC1s and mregDCs, such as IL12B and FLT3.

To further understand differences between mregDCs and cDC1/cDC2, we performed trajectory analysis[31], regulon (TF and its targets) inference[32], and immune response enrichment[33] inference for the three subtypes. Trajectory analysis revealed that both cDC1 and cDC2 possess the potential to transition into mregDCs (**Extended Fig. 4C**), consistent with findings from experimental studies using mouse cDCs[16]. Despite its lower expression in mregDC compared to cDC1, IRF8 exhibited the highest regulon specificity score in mregDC, indicating its potential role in mediating the transition from cDC1 to mregDC (**Extended Fig. 4D**). Other top regulons included those associated with NF-κB signaling (REL, NFKB1, NFKB2), AP-1 signaling (FOSB, JUND, FOSL2), and oxidative stress response (MAFG, NFE2L2). IRF1, another regulon enriched in mregDC, has been implicated in driving antitumor immunity in mouse models through its control by NF-κB signaling[34]. Additionally, IKZF1, another enriched regulon in mregDC, is known to regulate DC function in humans[35]. KLF3 and KLF6 were also among the top enriched regulons in mregDC. Notably, KLF4, a member of the same Krüppel-like factor family, has been reported to promote Th2 cell responses in IRF4-expressing cDCs[36]. Immune response enrichment[33] indicated that mregDCs exhibited transcriptional responses to IL1β, TNFα, IL12, IFNβ, GM-CSF, TSLP, and IL18, while cDC1 showed enrichment for Leptin, Flt3l, LIF, and IL21 (**Extended Fig. 4E**). GM-CSF[37] and TSLP[38] are known to promote cDC maturation and activation, while Flt3l is crucial for cDC precursor development and cDC maintenance[39] and IL21 was shown to inhibit DC activation and maturation[40]. Pro-inflammatory cytokines such as IL1β, TNFα, IL12, IFNβ appeared to influence mregDCs as well.

Differential interactome between mature and migratory cDCs and other cDCs

To examine unique cellular interactions between the three cDC subtypes and other cell populations, we conducted cell-cell communication analysis utilizing ligand-receptor co-expression patterns[41], revealing immune-stimulatory and -regulatory roles of mregDCs in the TME, and the survival and activation signals they receive from T cells and other myeloid cells. We annotated interactions with varying inferred activities in mregDC compared to other cDCs or those exclusively present in mregDCs (**Supplementary Table 8,9**). Notably, CD8 T-cells, CD4 T-cells, and monocytes/macrophages exhibited the highest number of such interactions with cDCs, either as sources or targets (**Extended Fig. 4F**). For CD8 T-cells, mregDC exhibited heightened interactions with CD8 exhausted memory T cells (CD8 Texme), exhausted CD4 T cells (CD4 Tex), regulatory T cells (Treg), and M1 macrophages through CD274 (PD-L1) and PDCD1 (PD-1) interactions (**Fig. 4G, Supplementary Fig. 4D**). This finding underscores the significance of these interactions in mediating ICI response, particularly anti-PD-1 treatment. Specific molecular interactions were exclusive to mregDCs, including interaction between the up-regulated CCL19 cytokine in mregDCs and CCR7-expressing CD8 effector and exhausted T cells, as well as early activated CD4 T cells (CD4 CD69+ T), suggesting potential recruitment of these T cells by mregDCs. Additionally, co-immunoregulatory interactions such as TIGIT-PVR, PDCD1LG2 (PD-L2)-PDCD1 (PD-1), and CD200-CD200R1 were observed between mregDCs and exhausted CD8 T cells with high heat shock gene expression (CD8 Tex/HS), CD4 CD69+ T cells, Tregs, CD8 effector memory T cells (CD8 Tem), CD4 NKT cells and M2 macrophages (**Fig. 4G, Supplementary Fig. 4D**). The interaction involving PD-L2 and PD-1 could represent another site of action with anti-PD-1 treatment. Apart from co-immunoregulatory signals, we identified interactions between CD70 and CD27 on mregDCs and naive and memory CD4 T cells, potentially mediating the co-occurrence of mregDCs and naive CD4 T cells (**Fig. 2F**). We also observed decreased levels of prostaglandin E2 interaction with PTGER2 on memory CD4 T cells (**Fig. 4G**), suggesting inhibition of Th2 differentiation for these cells[42], aligning with the lower levels of Th2 response genes seen in mregDCs (**Supplementary Fig. 4B**). Additionally, mregDC also up-regulated the interaction of RARRES2 (chemerin) and CMKLR1 with non-classical monocytes (**Supplementary Fig. 4D**), and indeed

chemerin has been reported to act as a tumor suppressive cytokine in mouse melanoma models by recruiting innate immune cells into the TME[43].

Conversely, TNFSF9 (4-1BBL) and TNFRSF9 (4-1BB) exhibited co-expression among CD8 Tn, CD8 Texme, CD8 GNLY+ Tex, and mregDC (**Extended Data Fig. 4G**). The interaction between CD8 Tn and mregDC is particularly noteworthy, given that 4-1BB has been demonstrated to serve as a survival factor in DCs, regulating DC immunogenicity and DC-T interaction[44]. Another ligand-receptor interaction notably up-regulated between mregDC and all CD8, CD4, monocyte and macrophage subtypes except CD8 Tex/HS was TNFRSF11B and TNFSF10 (TRAIL; **Extended Data Fig. 4G, Supplementary Fig. 4E**). TNFRSF11B is known to compete for TRAIL binding to death-activated receptors, offering a mechanism to prevent apoptosis in the presence of TRAIL[45]. Given the previously observed up-regulation of death receptor signaling in mregDCs, the heightened expression of TNFRSF11B could signify another pro-survival strategy for mregDC. Simultaneously, TNFSF12 (TWEAK) expressed by CD4 Tregs likely interacted with TNFRSF25 on mregDCs (**Extended Data Fig. 4G**), which was suggested to modulate the innate response and its transition to adaptive Th1 immunity[46]. We also observed an up-regulated co-expression of NRP2 (neuropilin-2) and SEMA3C between classical monocytes and mregDCs (**Supplementary Fig. 4E**). Neuropilin-2 is known to play an essential role in the activation of DCs[47].

Epigenomic landscape of mature and migratory cDCs

For the subset of 15 samples with snATAC-seq data, we performed label transfer[48] from the scRNA-seq atlas to annotate major cell types in the epigenomic space (**Fig. 5A**). Given the significance of mregDC in mediating ICI response, we isolated cDCs from both scRNA-seq and snATAC-seq data, integrated them into a unified UMAP space, and identified cDC subtypes through unbiased clustering and RNA-based annotations (**Fig. 5B**). Using differential accessibility analysis, we found distinct regions between mregDC and cDC1, and mregDC and cDC2, with more than double the number of differentially accessible regions (DARs) observed between mregDC and cDC2 compared to mregDC and cDC1 (2615 vs. 1186; **Fig. 5C, Supplementary Table 10**). For accessible regions with specific activities in mregDC, cDC1 showed a higher global activity correlation across these peaks than cDC2 (**Extended Data Fig. 5A**). Despite the limited number of cDC1 and mregDC cells in the ATAC data, our results suggest a more pronounced epigenomic change between mregDC and cDC2. Correspondingly, DARs between mregDC and cDC2 are significantly enriched in more biological processes compared to DARs between mregDC and cDC1 (**Extended Data Fig. 5B,C, Supplementary Table 11**), consistent with the diverse biological pathways enriched in DEGs between mregDC and cDC2 observed in our RNA data (**Fig. 4D,F**). The DARs with higher activities in mregDC compared to cDC1 or cDC2 were enriched in motifs for all five members of the NF-κB transcription factor family, including RELA, RELB, REL, NFKB1 and NFKB2 (**Fig. 5D**). Although we did not find motifs significantly enriched in DARs with higher activities in cDC1, motifs for the C/EBP family of TFs were significantly enriched in DARs showing higher activities in cDC2 (**Fig. 5D**). Notably, enhancer accessibility for IL15, FSCN1, and DUSP22—genes crucial for DC functions—were identified only in mregDCs (**Fig. 5E**), indicating potential epigenomic reprogramming during cDC maturation and activation. Both FSCN1 and DUSP22 enhancers contain motifs for the NF-κB TF family, highlighting the important role of NF-κB signaling in mediating DC maturation. Additionally, we pinpointed enhancers for KDM2B, implicated in regulating IL6 expression[49]; GLS, glutaminase 1, a prognostic biomarker linked to DCs and immunotherapy response in breast cancer[50]; and CCR7, pivotal for DC migration and lymph node homing (**Extended Data Fig. 5D**).

Molecular and cellular factors associated with mature and migratory cDC proportions

Having established an association between mregDC proportion and ICI response, and its predictive value for patients' PFS, with the recognition of mregDC as a distinct cDC subtype with unique transcriptional and epigenomic signatures, we next shifted our focus to understanding the molecular and cellular determinants influencing mregDC proportions within the TME. To achieve this, we stratified the cohort into two groups based on mregDC levels: high vs. low, using the median mregDC proportion within cDC as a threshold (a median value of 18.5%, consistent with the survival analysis). For each cell type and subtype, we identified cell states associated with mregDC proportion and DEGs characterizing the mregDC-associated cell state, while adjusting for sample- and cell-level covariates (**Fig. 6A**). Subsequently, we investigated the enriched biological pathways and immune responses based on these DEGs. Additionally, we examined the differential cell-cell interactions between high and low mregDC samples using logistic regression models, accounting for sample-level covariates.

At the cell type level, tumor cells, fibroblasts, and B cells exhibited the highest number of DEGs linked to mregDC proportions (**Fig. 6B**). Due to cell subtype heterogeneity, DEGs identified at the cell type level may reflect varying proportions of cell subtypes within the cell type across the two groups. Indeed, we observed this for B cells, where the proportion of naive B cells correlated with mregDC proportions, and naive B cells were the predominant subtype within B cells in terms of abundance (**Fig. 2F**). However, for tumor cells and fibroblasts, a significant number of DEGs persisted at the cell subtype level, indicating that subtype-specific DEGs primarily drove the cell type-level differences (**Extended Data Fig. 6A**). Interestingly, for the translation initiation tumor program, correlated with mregDC proportion (**Fig. 2F**), we identified only 10 DEGs (**Extended Data Fig. 6A**), highlighting the model's specificity.

Analyzing the top DEGs for each cell type, we observed upregulation of CCR7 in cDCs among mregDC high samples, consistent with its role as an mregDC marker (**Fig. 6C, Supplementary Table 12**). At the cell subtype level, MHC class II genes were upregulated in mregDC high samples across various tumor programs, including HLA-DRB1 in tumor cell cycle G1/S and respiration programs, and HLA-DQA2 in tumor interferon MHC-II program (**Extended Data Fig. 6B, Supplementary Table 13**), indicating the immunogenic potential of these tumor programs in mregDC high samples. Notably, melanoma dedifferentiation marker NGFR and drug resistance marker AXL were upregulated in the tumor cell cycle G2/M program, suggesting potential interactions with mregDC that remain to be elucidated. In fibroblasts, inflammatory fibroblasts exhibited upregulation of CCL21, while myofibroblasts upregulated IL24 and CXCL10 in mregDC high samples (**Extended Data Fig. 6C**). These cytokines and chemokines possess proinflammatory and anti-tumor properties, indicating an anti-tumor microenvironment in mregDC high samples.

These cell type-specific DEGs showed enrichment in upregulated ECM pathways in tumor cells and fibroblasts, and downregulated cell cycle pathways across various cell types including tumor, other T, NK, B, cDC, and pDC cells (**Fig. 6D**). Additionally, fibroblasts exhibited downregulation in muscle contraction-related pathways and the VEGFα VEGFR2 signaling pathway, indicating a shift from myofibroblasts to inflammatory fibroblasts in mregDC high samples. Subtype-level analysis revealed upregulation of the ECM pathway in the tumor translation initiation and unfolded protein response programs, while it was downregulated in several other tumor programs such as tumor interferon/MHC-II and stress programs (**Extended Data Fig. 6D**). The tumor respiration program displayed upregulation in PD-1 signaling and antigen processing and presentation pathways, suggesting its involvement in anti-PD-1 response and its association with mregDCs. Similarly, the tumor stress program upregulated PD-1 signaling pathway and additionally showed upregulation in the costimulation by the CD28 family pathway, indicating its potential to induce robust T cell responses directly. Inflammatory fibroblasts and myofibroblasts contributed to increased ECM pathway activity at the cell subtype level, while inflammatory fibroblasts exhibited upregulation of proinflammatory and profibrotic mediators in mregDC high samples (**Extended Data Fig. 6E**).

Furthermore, the tumor stress program and inflammatory fibroblasts showed specific cell-cell communications in mregDC high samples (**Supplementary Fig. 5A,B; Supplementary Table 14**). The tumor stress program was predicted to interact with cDC2 via HEBP1 and FPR3, and with M1 macrophage via CD99 and PILRA. Inflammatory fibroblasts were predicted to interact with cDC2 via HEBP1 and FPR3, and with effector memory and exhausted memory CD8 T cells, double negative NKT cells, and other T cells via the TNC and integrin a4b1 complex (**Supplementary Fig. 5B**). Cathepsin D is known to process HEBP1 to produce F2L, a high-affinity natural agonist for FPR3[51], which is expressed throughout human DC maturation and may regulate DC trafficking during antigen uptake and processing[52]. PILRα, encoded by PILRA, controls monocyte mobility by regulating integrin signaling and inhibiting CD99-CD99 binding[53], while anti-CD99 antibody therapy was shown to trigger myeloid cell recruitment *in vivo*[54]. α4β1 integrin (also known as very late antigen-4, VLA-4) is expressed on leukocytes and mediates various cellular functions[55], while TNC induces cytokine production via integrin α4β1[56]. Overall, the tumor stress program and inflammatory fibroblasts secrete ligands that impact the functions of cDCs, other myeloid cells, and lymphoid cells in mregDC high samples, potentially contributing to the transition of cDC1 and cDC2 into mregDCs.

Discussion

We compiled a single-cell atlas of metastatic melanoma from 16 responding and 23 non-responding tumors, comprising over 200,000 cells across 55 annotated subtypes. Using this atlas, we identified six cellular programs with correlated subtype proportions, indicating regulatory relationships within the TME. We validated these cellular programs by integration with four previously published single-cell studies[7–10], demonstrating

distinct anti-tumor and pro-tumor functions based on known cell subtype characteristics. Notably, we observed a higher relative proportion of mregDCs in responders compared to non-responders to ICI treatment. This observation was confirmed in an independent ICI-treated bulk meta-cohort. When combining mregDC proportion with the TCF7+/- CD8 T cell ratio, we stratified patients' survival across treatments. Furthermore, our characterization of mregDCs using scRNA-seq and snATAC-seq data indicates their origin from cDC1, driven by intrinsic TFs like IRF8, and extrinsic factors such as pro-inflammatory cytokines (IL1β, TNFα, IL12 etc.), along with ECM genes from specific tumor cells and fibroblasts. These factors potentially induce epigenomic reprogramming of naive cDCs, leading to the adoption of new phenotypes and functions.

We identified specific cellular ligand-receptor co-expressions between mregDCs and T cells and other myeloid cells, potentially explaining ICI response in mregDC high samples. Our analysis revealed that mregDC proportions correlated with naive CD8 T, naive CD4 T, and naive B cell proportions in the TME, indicating its involvement in immune infiltration. At a molecular level, we predicted mregDCs interacting with naive CD4 T cells via CD70 and CD27, and with naive CD8 T cells via 4-1BB and 4-1BBL. CD27, a T cell costimulatory molecule, is known to support antigen-specific expansion of naive T cells[57], while CD70 expressed on cDCs has been shown to promote the development of CD4 T cells producing various effector cytokines[58]. Additionally, the interaction between CD27 on naive CD8+ T cells and CD70 on APCs has been recently shown to determine T cell memory fate, with CAR-T cells generated with CD27 costimulation showing superior antitumor efficacy[59]. Moreover, 4-1BB, besides its role in DC maturation and pro-survival signaling[44,60], has shown promise in enhancing antitumor immunity in clinical trials by dual targeting and conditional stimulation of CD40 (inducing DC maturation) and 4-1BB (NCT04083599)[61]. These molecular interactions underscore the intimate relationship between mregDCs and naive T cells, providing additional DC-T targets beyond CD40-CD40L. However, the interpretation of these costimulatory signals needs to consider regulatory signals such as PD-1/PD-L1 and IDO1, which have been shown to affect the proliferation and effectiveness of naive CD8 T cells and induce the differentiation of naive CD4 T cells into Tregs using *in vitro* co-culture assays[62,63]. Additionally, our investigation into cell type-specific molecules associated with mregDC proportion in the TME highlighted the potential regulatory roles of the tumor stress program and inflammatory fibroblast through transcriptomic and cell-cell communication changes.

The higher proportion of mregDCs observed in ICI-responding tumors, both in the single-cell dataset and a large ICI-treated bulk meta-cohort, is consistent with the expression of a direct target of anti-PD-1 treatment on their surface. Studies in mouse models have shown that PD-L1 on cDC1s attenuates T cell activation and regulates response to ICI[27]. Additionally, in a cohort of pembrolizumab-treated breast cancer patients, the relative frequency of mregDCs positively correlated with T-cell expansion following anti-PD-1 treatment, and mregDCs supported T-cell function in responders at baseline and during treatment[26]. Previous findings also suggested that mregDCs may be associated with better patient outcomes, as confirmed by the presence of mregDC cell markers associated with improved overall survival in melanoma patients[64]. Furthermore, the enrichment of a CCR7+ DC signature (mregDC) has been linked to improved survival in lung cancer, cutaneous melanoma, breast, and colorectal cancer by analyzing 4,045 human solid tumor transcriptomes from the TCGA[65]. In our study, while we did not find mregDC proportion alone as a pan-treatment pro-survival biomarker, combining mregDC proportion and TCF7+/- CD8 T ratio, a previously reported ICI response marker[9], allowed us to predict patient survival across treatments. Notably, these two cell subtypes were recently found to be enriched in spatially organized stem-immunity hubs in human lung cancer, associated with response to immunotherapy[66].

Employing both scRNA-seq and snATAC-seq data from a substantial cohort of cDCs within the human melanoma TME, we meticulously delineated the three subtypes: cDC1, cDC2, and mregDC. Our investigation unveiled that mregDCs share transcriptional and epigenetic resemblances with cDC1s rather than cDC2s, suggesting their probable derivation from cDC1, in line with recent pan-cancer insights[67]. Moreover, we pinpointed TFs with heightened activity in mregDCs, notably IRF1, IKZF1, KLF3, and KLF6, urging deeper exploration of their roles in orchestrating the mature and regulatory phenotype. Our analysis of transcriptional signatures linked with various cytokines revealed an enrichment of proinflammatory cytokines (IL1β, TNFα, IL12, IFNβ), alongside cytokines pivotal for DC maturation and activation (GM-CSF, TSLP, IL18) in mregDCs, aligning with expectations. Additionally, we noted an enrichment of leptin, LIF, and IL21 in cDC1 compared to mregDC, highlighting cytokines for future investigation. More importantly, we uncovered that transcriptional alterations in tumor cells and fibroblasts correlated prominently with mregDC proportions in the TME, with both

cell types upregulating ECM pathways in mregDC high samples. These findings gain significance as ECM proteins are known to influence DC maturation[68]. Furthermore, we identified a specific molecular interaction, HEBP1-FPR3, between tumor cells/fibroblasts and DCs, potentially regulating DC trafficking through ECM[52].

Overall, our study reveals a rich repository of single-cell profiles from human metastatic melanomas, coupled with extensive clinical data, and underscores the critical role of mregDCs in shaping the TME and their potential as prognostic markers and therapeutic targets in melanoma treatment.

Limitations of study

In this study, our samples displayed significant clinical heterogeneity, including variations in treatment types and stages. While we attempted to address these variations computationally, a larger single-cell cohort would enhance the robustness of molecular and cellular correlates with patient responses and survival benefits. For communication analysis, integrating orthogonal data types like imaging and experimental approaches such as *in vitro* co-culturing systems and *in vivo* tracer methods would be invaluable in substantiating the predicted cell crosstalk.

Acknowledgements

We thank past and present members of the Boland, Kellis, Liu, and Rai laboratories for thoughtful scientific discussions. We thank Natalie D'Amore, Eric Lightcap and Sarah Hesse for discussions and feedback on sample collection, sample processing and data analysis. This work was supported by Takeda Pharmaceuticals, Boston, MA, USA (M.K.), the Adelson Medical Research Fund (G.M.B.), Bill and Emma Roberts MGH Research Scholar (G.M.B.), the Society for Immunotherapy of Cancers (David Liu), the Doris Duke Charitable Foundation Clinical Scientist Training Program (David Liu)...

Author Contributions

This study was designed and directed by G.M.B. and M.K. D.T.F. and T.S. compiled clinical information. L.H., K.G., and D.T.F. coordinated sample acquisition. L.H. and K.G. performed scRNA-seq and snATAC-seq experiments. J.Y., C.W., D.F., L.C., A.Y.H., E.J.R., and R.T. performed data processing and computational analysis. A.Y.H. performed analysis in the bulk meta-cohort. D.L. designed and directed the bulk meta-cohort study. S.K.Y., W.D., K.P.B., and K.R. provided scientific feedback. J.Y., C.W., D.F., G.M.B., and M.K. wrote the manuscript.

Declaration of Interests

The authors declare that they have no conflict of interest.

Figure Legends

Figure 1. Characterization of cells in human metastatic melanoma tumors. A, Demographic summary of the 39 samples included in this study. Pfs, progression-free survival; os, overall survival; NR, non-responder; R, responder. **B**, Uniform manifold approximation and projection (UMAP) embedding of all the cells from the 39 samples, after quality control, with each color representing a cell type. **C**, Dotplot showing average normalized expression and percent normalized expression of marker genes across cell types.

Figure 2. Cell subtypes and their relative proportion correlations in the tumor microenvironment. A, UMAP embedding of tumor cells annotated with meta-programs according to Gavish *et al*. **B**, Heatmap of the top marker genes for each of the identified tumor meta-programs. **C-E**, UMAP embedding of myeloid cell subtypes (**C**), CD8 T-cell subtypes (**D**), and CD4 T-cell subtypes (**E**). The cell subtypes known for their anti-tumor functions were delineated with dotted outlines. **F**, Heatmap illustrating correlation coefficients among the relative proportions of cell subtypes in relation to their corresponding cell types across all study samples. We identified clusters/modules by segmenting the hierarchical clustering tree at the red line and assigned annotations based on the known functions of the cell subtypes within each cluster or module.

Figure 3. Mature and regulatory cDCs associated with ICI response and patient survival. A, Boxplots comparing relative proportions of four subtypes between ICI non-responders and responders. Each dot represents a sample, with its color corresponding to the type of ICI and its shape corresponding to the melanoma subtype. **B**, Survival plots for samples only treated with ICI and split by the median value of mregDC relative proportion. **C**, Survival plots for all samples and split by the median values of both mregDC relative proportion and TCF7+ CD8 T ratio. **D**, Boxplot comparing mregDC signature scores, calculated using ssGSEA, between non-responders and responders in 274 ICI-treated bulk RNA-seq samples. **E**, Survival plots for the 274 bulk RNA-seq samples split by the median value of their mregDC scores. P values for boxplots

were calculated using the Wilcoxon Rank Sum test. P values for survival plots were calculated using the Log Rank Sum test. NR, non-responder; R, responder; combo, anti-PD-1+anti-CTLA-4; PFS, progression free survival; OS, overall survival.

Figure 4. Transcriptional landscape and interactome of cDC subtypes. A, UMAP embedding of cDCs colored by the subtypes. **B**, Violin plots of canonical marker genes for cDC1, cDC2 and mregDC. **C,E**, Volcano plots showing differentially expressed genes (DEGs) between mregDC and cDC1 (**C**) and between mregDC and cDC2 (**E**). An adjusted P value of 0.001 was used to call significant DEGs. Examples of genes with mregDC-specific enhancers were colored in green, which were mentioned in Figure 5. **D,F**, Networks of enriched terms for DEGs up- or down-regulated in mregDC compared to cDC1 (**D**) or cDC2 (**F**). **G**, Dotplots illustrating inferred cell-cell communications by CellPhoneDB[41] either with differential activities between mregDC and other cDC or exclusively detected in mregDC. The left and right panels plotted interactions with cDC expressing ligands and CD8 or CD4 T-cell expressing receptors, respectively. P values for volcano plots and dotplots were calculated using the Wilcoxon Rank Sum test.

Figure 5. Epigenomic landscape of cDC subtypes using snATAC-seq data. A, UMAP embedding of snATAC-seq cells with cell type labels transferred from scRNA-seq data. **B**, Co-embedding of cDCs from scRNA-seq and snATAC-seq data, with colors corresponding to assays (left) or subtypes (right). **C**, Differentially accessible regions between mregDC and cDC1 (top), and mregDC and cDC2 (bottom). The p value cutoff is 0.01. **D**, Motifs enriched in differentially accessible regions between mregDC and cDC1 (left), and mregDC and cDC2 (right). Significantly enriched motifs were marked with an asterisk (adjusted p-value <=0.05). **E**, Track plots comparing normalized number of reads across cDC subtypes underlying enhancers associated with genes important for cDC functions. mDC is short for mregDC in some figure panels due to space constraints. A peak is colored orange if it contains motifs for members of the NF-κB transcription factor family.

Figure 6. Cell type-specific molecular factors associated with mregDC proportions. A, Illustration of sample splitting, model used, and downstream analyses performed to identify cell type-specific molecules associated with mregDC proportion. **B**, Bar plots showing the number of cell type-specific differentially expressed genes (DEGs) significantly upregulated or downregulated in mregDC high samples, detected by a linear mixed model. **C**, Aggregated volcano plots across cell types showing DEGs passing the adjusted P value threshold in red and the rest of genes in gray. The top three genes with large average log2 fold changes in both directions are labeled. **D**, Dot plots illustrating the top three pathways enriched by the up and downregulated DEGs for each cell type. The pathway names were colored by biological themes.

Extended Data Figure 1. Visualization of the scRNA-seq atlas. Uniform manifold approximation and projection (UMAP) embedding of all the cells from the 39 samples, after quality control, with each color representing a compartment (**A**), a sample (**B**), a melanoma subtype (**C**), a treatment group (**D**), and patient's response to treatment (**E**). ICI, immune checkpoint inhibitor; ICI combo, anti-PD1 plus anti-CTLA4; NR, non-responder; R, responder.

Extended Data Figure 2. Cell subtype markers and pairwise correlations between certain cell subtypes. A, On the left, UMAP embedding of all the tumor cells. Each color represents either a specific tumor meta-program or cells that did not pass the quality control in this analysis. On the right, violin plots displaying the number of genes per cell, categorized by their inclusion in different tumor meta-programs or unannotated cells. **B-D**, Dotplot showing average expression and percent expression of marker genes for the myeloid cell subtypes (**B**), CD8 T-cell subtypes (**C**), and CD4 T-cell subtypes (**D**). **F-I**, Scatterplots depicting the pairwise correlations between two cell subtypes within module 1 (**F**), module 2 (**G**), module 3 (**H**), and module 4 (**I**). Each data point represents a sample, distinguished by shape representing melanoma subtype and color indicating the treatment group. Pearson correlation coefficients and p-values are provided within each plot.

Extended Data Figure 3. Cell subtype association with ICI response and patient survival. A, Boxplots comparing relative proportions of selected cell subtypes between ICI non-responders and responders. Each dot represents a sample, with its color corresponding to the treatment group and its shape corresponding to the melanoma subtype. **B** and **C**, Survival plots for samples treated with ICI (**B**) or all samples (**C**) and split by the median value of mregDC relative proportion. **D**, Scatterplot correlating mregDC relative proportion and TCF7+ CD8 T ratio using all samples. Each dot corresponds to a sample and is colored by treatment response. **E**, Boxplot comparing TFC7+ versus TCF7- CD8 T cell ratio between ICI non-responders and responders. **F**, Survival plots for samples treated with ICI only and split by the median value of TCF7+ versus -

CD8 T cell ratio. P values for boxplots were calculated using the Wilcoxon Rank Sum test. P values for survival plots were calculated using the Log Rank Sum test. R-square and P values for scatterplots were calculated using the Pearson Correlation test. NR, non-responder; R, responder; combo, anti-PD-1+anti-CTLA-4; PFS, progression free survival; OS, overall survival.

Extended Data Figure 4. Additional transcriptional characterization and cell-cell communication of cDC subtypes. A, UMAP embedding of cDCs colored by sample. **B**, Scatterplot showing cDC1, cDC2 and mregDC scores per cell based on the marker genes reported in Maier *et al*. **C**, CytoTrace stream embedding overlaid on UMAP showing converging transition paths from cDC1 and cDC2 to mregDC. Arrows show state transition directions. **D**, Scatterplot of mregDC regulon specificity scores inferred by SCENIC. Top 20 regulons are highlighted. **E**, Barplot showing cytokines with transcriptional signatures enriched in mregDC relative to cDC1, based on Cui *et al*[33]. **F**, Bar plots showing the number of differential or exclusive interactions by cell type, with the top panel corresponding to cDC as source and the bottom panel cDC as target. The bars are colored by the subtypes in each cell type. **G**, Dotplots illustrating inferred cell-cell communications either with differential activities between mregDC and other cDC or exclusively detected in mregDC. The left and right panels plotted interactions with cDC expressing receptors and CD8 or CD4 T-cell expressing ligands, respectively. P values for dotplots were calculated using the Wilcoxon Rank Sum test.

Extended Data Figure 5. Additional epigenomic analysis results for cDC subtypes. A, Overall activity correlation across accessible regions specific to mregDC in cDC1 and cDC2. **B,C**, Gene ontology (GO) networks showing the GO terms enriched by the differentially accessible regions (DARs) between mregDC and cDC1 (**B**), and mregDC and cDC2 (**C**). The enrichment analysis was carried out using the GREAT program[69]. **D**, Track plots comparing normalized number of reads across cDC subtypes underlying enhancers associated with genes important for cDC functions. mDC is short for mregDC in some figure panels due to space constraints. A peak is colored orange if it contains motifs for members of the NF-κB transcription factor family.

Extended Figure 6. Cell subtype-specific molecular factors associated with mregDC proportions. A, Bar plots showing the number of cell subtype-specific differentially expressed genes (DEGs) significantly upregulated or downregulated in mregDC high samples, detected by a linear mixed model. **B,C**, Aggregated volcano plots across tumor programs (**B**) or fibroblast subtypes (**C**) showing DEGs passing the adjusted P value threshold in red and the rest of genes in gray. The top three and ten genes with large average log2 fold changes in both directions are labeled, respectively. **D,E**, Dot plots illustrating the top three pathways enriched by the up and downregulated DEGs for each tumor program (**D**) or fibroblast subtype (**E**). The pathway names were in bold if discussed in the text.

Materials and Methods

Patient cohorts for single-cell analysis

The metastatic melanoma samples for this study were obtained from Massachusetts General Hospital by G.M.B. under the DF-HCC protocol 11-181 (PI: G.M.B.). Our study focused on annotated metastatic tumors treated with ICIs, targeted inhibitors, other immune therapies, or their combinations as primary treatment. Patient age, progression-free survival (PFS), and overall survival (OS) were calculated from the treatment start date. Lesional response was assessed using RECIST 1.1 criteria.

Single-cell RNA-sequencing and preprocessing

We enzymatically digested and dissociated fresh tumor samples according to tissue dissociation kit protocols using the gentleMACS™ Dissociator (Miltenyi). Dissociated tissues were filtered, centrifuged, and the isolated cells were resuspended in 0.1% BSA in PBS and immediately processed for the generation of single-cell RNA (scRNA) libraries using the droplet-based RNA sequencing technology. Briefly, 5000-6000 cells were profiled per sample using the Chromium Single Cell 3' RNA reagent kit v3 (three samples were processed using kit v2) according to the 10X Genomics protocol. The generated cDNA libraries were indexed, pooled, and sequenced in batches using the NovaSeq 6000 S2 system and reagent kits (100 cycles; Illumina). We received the sequences, mapped the reads against the GRCh38 human reference genome, and quantified the read counts using Cell Ranger pipeline version 3.1.0 (10x Genomics).

Single-nucleus ATAC-sequencing and preprocessing

We performed snATAC-seq using the Chromium single cell ATAC v1 chemistry from 10x Genomics with the target of 5000 nuclei per sample. Then the libraries were profiled using the Novaseq S2 (Illumina) technology. We aligned and quantified the libraries using the 10X cellranger-atac-2.0.0 pipeline.

Single-cell RNA-seq data analysis

Quality control, dimensionality reduction, clustering and cell type annotation: We used CellBender[70] to remove ambient RNA in each sequencing library and called multiplets using Scrublet[71]. We then used standard pre-processing workflow from Seurat (v4)[72] to prepare the scRNA-seq dataset. Single cells with <200 genes or >6000 genes or >10% of reads mapping to the mitochondrial genome were removed. Data normalization and scaling was performed using SCTransform[48], to adjust for sequencing depth and remove mitochondrial mapping percentage as a confounding variable. We then merged the libraries and performed principal component analysis (PCA) using the genes detected in all samples. After obtaining the low-dimensional embeddings, we performed Uniform Manifold Approximation and Projection (UMAP) on the top 40 principal components to visualize the dataset. We then constructed a k Nearest Neighbor (kNN) Graph in the top 40 principal components space and clustered cells using the Louvain algorithm. In all the datasets, we used the default parameter k = 20 and resolution parameter ranging from 0.2 to 1.4 and proceeded with the lowest resolution that sufficiently highlighted the biological differences between clusters. We annotated each cluster using known cell-type specific markers. To identify proliferating cells, we used the CellCycleScoring function to calculate the S phase score and G2M phase score for each cell. To identify tumor cells, we used inferCNV (https://github.com/broadinstitute/inferCNV) to infer copy number alterations from potential tumor clusters in comparison to normal cell clusters.

Cell type-specific subclustering: A cell type of interest was subsetted from the object containing all cells from the 39 samples, which passed quality control metrics described in the previous method section using the subset function. We then ran SCTransform[48] on the raw counts of the subset, with the default “v2 regularization” and the “vars_to_regress” parameter equal to the percentage of mitochondrial genes. After applying SCTransform, PCA was applied on the scaled data. Next, to ensure integration of cells by cell subtypes rather than by the technical variation across samples, we used Harmony[73], an algorithm that projects cells into a shared embedding in which cells group by cell states rather than dataset-specific conditions, different samples in our case. Finally, non-linear dimensionality reduction was applied with UMAP, using the first 30 dimensions from the reduction from Harmony, to visualize the cells in 2D.

Cell subtype annotation: The identification of subtypes for each cell type was determined by two approaches: 1) a priori knowledge of specific markers for subtypes revealed in the literature, and 2) graph and/or density-based clustering algorithms to cluster groups of cells of the same cell type followed by identification of differentiating markers among clusters. Both approaches were used concurrently to find the best partitions of subtypes, as detailed below: 1) Using known markers for specific subtypes: Through extensive literature search, markers distinguishing cell subtypes were visualized using the Seurat function FeaturePlot to identify patterns of the expression of certain markers for the differentiation and assignment of subtypes. 2) Applying clustering methods to delineate subtypes: Clustering methods were applied to determine subtypes within cell type subsets and could be of either of the following methods: a) The FindClusters function in Seurat identified clusters of cells by constructing a shared nearest neighbor (SNN) graph from k-nearest neighbors (kNN). Then the modularity function was optimized using the Louvain algorithm, which finds non-overlapping clusters from networks to determine the clusters. The default parameters were kept while varying the resolution to match the expected number of subtypes within the cell type (higher resolution = more clusters). b) Density-Based Spatial Clustering of Applications with Noise (DBScan), is a density-based clustering algorithm that uses an embedding of points (in our case the UMAP projection) to cluster points by how close or far they are from one another. The R package dbscan was used to find clusters, in which the “eps” parameter was set to the radius of neighboring points and the "MinPts” parameter, which specified the threshold for the minimum number of neighbors within the radius. By assigning points by these parameters, clusters as well as outlier points were found by the algorithm. 3) Validation of subtypes through differential gene expression analysis: Clusters could be compared against each other by finding DEGs between one or more clusters. We used FindMarkers to identify DEGs among the various clusters to verify that the clusters differentially express the known markers of interest from literature or discover markers to confirm the presence of a subtype. This was applied when the marker expression was not very apparent merely by observation through FeaturePlot. Once clusters were determined, the subtype annotations were integrated back into the original object containing all cells from the 39 samples. Cells that passed quality control metrics but did not cluster with any annotated subtypes were found using dbscan. Outlier cells were discarded from the finalized object.

Subtyping of malignant cells: We used a different approach, as described in Gavish *et al.*[18], to uncover "meta-programs" of tumor cells, with each uniquely describing a distinct cellular state through a gene set. Each cell was assigned to the meta-program for which its sum of gene activities for the specific meta-program's genes was the maximum among all meta-programs tested and meeting defined constraints. Overall, a minimum score of 0.03 was enforced to yield 60.1% of tumor cells that would be assigned to a meta-program (to roughly match the threshold of 56.4% used by Gavish *et al.*[18]). After assignment, cells that did not reach the threshold for any of the meta-programs (default score for assignment = 1) or did not have the minimum number of genes to test for any meta-program (default number of genes = 25) were assigned as NA. The code to run the meta-program distribution is at https://github.com/tiroshlab/3ca/blob/main/ITH_hallmarks/MPs_distribution/MP_distribution.R.

Cell subtype proportion correlation analysis: Cell type and subtype abundances were calculated by sample. Relative subtype proportion was calculated by dividing the abundances of a subtype by its corresponding cell type. Given an input proportion by patient sample matrix, Pearson correlation was calculated for every pair of subtype proportions across samples using the Python corr function from the pandas library. Correlations of proportions where the cell type was not present in a sample were excluded from the analysis, as it would lead to a "division by 0" error. Groups of similar correlations were clustered together for the generation of the correlation matrices by measuring the distances between correlations and making clusters based on the distances, which was executed using the linkage and fcluster functions in the SciPy package in a wrapper developed by Yegelwel (https://wil.yegelwel.com/cluster-correlation-matrix/). After visual inspection of the correlation matrices, correlation plots highlighting the relationship between pairs of highly correlated subtypes were generated with an associated p-value to determine the probability of the result, assuming that the correlation coefficient was truly 0.

Cell subtype proportion by response analysis: To evaluate subtype proportions stratified by responding and non-responding tumors, we generated boxplots to visualize the distributions and measured the difference in distributions using the Wilcoxon rank sum test. This test was computed by the wrapper function wilcox.test in R and using a two-sided alternative (no prior information determining which distribution would be higher) to determine whether the distribution of a certain subtype proportion was different between samples in the response or non-response groups. We also performed multiple analyses evaluating the distribution of subtype proportions on the different treatment group cohorts of samples from all treatments, samples treated with ICI, ICI-only treated samples, and samples treated with anti-PD1. P-values were labeled if it was less than 0.1, but we still evaluated significance based on a p-value less than 0.05.

Kaplan Meier survival analysis: For our analysis, survival curves between two groups of samples were compared, and their differences were evaluated for significance using the log-rank sum test. Kaplan Meier survival curves were generated in R using the libraries survival and ggsurvfit. The function Surv from survival combined the survival data and corresponding censored data, which was used as the response variable of the formula survfit2 model from ggsurvfit. The survival data was stratified by the proportions we evaluated survival by, which was passed as binarized values according to the chosen cutoff value with which to group samples. Log-rank testing was performed for each survival analysis, and p-values were calculated between the different groups using the internal function add_pvalue in ggsurvfit.

DEG and pathway analysis of cDC subtypes: To perform differential gene expression analysis comparing mregDC to the other cDC subtypes in a pairwise fashion, we applied FindMarkers on the SCTransform normalized gene expression of the cDC scRNA-seq subset and compared the subsets of mregDC and cDC1 or mregDC and cDC2 using a Wilcoxon rank sum test. A log fold change threshold of 0.01 was used, and the minimum percentage of cells with the detected gene was set to 10%. DEGs were selected using an adjusted p-value (Bonferroni method by default) of 0.001. We used Metascape[74] to identify the enrichment of pathway networks for the DEGs.

Trajectory, regulatory network and immune response inference for cDC subtypes: We leveraged the CytoTraceKernel function in the python package Cellrank to infer the CytoTrace pseudotime[75]. We analyzed the activated regulatory networks in cCD1, cDC2, and mregDC subtypes with SCENIC[32]. Starting with the raw count matrix as input, we used GRNBoost2 to find regulatory networks, which are sets of genes co-expressed with transcription factors (TFs). To remove false positives and indirect targets, we pruned the networks using RcisTarget, which identifies direct-binding targets with motif enrichment of the correspondent upstream regulator. Finally, we used AUCell to compute the regulon activity score (RAS) in each cell based on the

ranked expression value of genes in the regulon. To select regulons specific to mregDCs, we calculated the regulon specificity score, which reflects the entropy of RAS in cells across cDC subpopulations, for each detected regulon. The regulon specificity score ranges from 0 to 1, with a higher value indicating more specificity of the regulon. We then used the Immune Response Enrichment Analysis (IREA) tool to find enriched cytokine expression in mregDCs relative to cDC1s and cDC2s. We used DEGs between mregDCs relative to cDC1s and cDC2s as defined above (**Supplementary Table 6**). Then, the upregulated and downregulated DEGs were separately input into IREA, with “MigDC”, “cDC1” or “cDC2” selected as the cell type and score chosen as the method. We combined the outputs from both sets of DEGs, negating the enrichment score of the downregulated DEGs, and then filtering for significance (adjusted p-value <=0.05). We removed cytokines that were determined to be significantly expressed in both the upregulated and downregulated DEGs.

Cell-cell communication for cDC subtypes: To infer cell-cell communication, we used CellPhoneDB[41], which takes in single-cell transcriptomic data and compares gene expression values to a database of ligand-receptor interactions to statistically test the significance of those interactions. We performed CellPhoneDB analysis to find ligand-receptor pairs between the cDC subtypes (mregDC, cDC1 and cDC2) and all other subtypes existing in our dataset. To preserve the integrity of true interactions, CellPhoneDB was run by sample (38 times independently for each sample in our scRNA-seq dataset). A log-normalized RNA count matrix of the sample and the list of subtype annotations for each cell were given as inputs to the program. Using the statistical analysis method of CellPhoneDB (Method 2), interactions between subtypes were obtained and compared to a null distribution generated by random shuffling of the cell types into clusters. The method is sped up via a geometric sketching procedure[76]. All parameters were set to the default. We used the output of the significant_means field, which provided an average mean value for an interaction between two partners of two cell subtypes if the interaction was significant; otherwise, the mean was equal to 0. We then looked into the interactions between the cDC subtypes and the other cell types. With our interest being in mregDCs, we had two goals: 1) to find interactions that existed only between the mregDC subtype and non-cDC cell types and not between cDC1 or cDC2 and non-cDC cell types; and 2) find cDC to non-cDC interactions that were differentially expressed between the cDC subsets. Several thresholds were applied for each analysis: 1) Exclusive interactions were only considered if the mregDC to other non-cDC subtype interaction was significant in at least 3 samples. 2) To evaluate differentially expressed interactions, the Wilcoxon rank sum test was applied for the same ligand-receptor interactions expressed by cDC1, cDC2, and mregDCs. Wilcoxon rank sum p-value <0.05 was used to call the differential. This analysis was performed separately when evaluating interactions when the ligand was expressed on cDCs (cDCs as the source) or when the receptor was expressed on cDCs (cDCs as the target).

Single-nucleus ATAC-seq data analysis

Quality control, clustering and dimensionality reduction: For quality control, we kept cells with peak region fragments between 5000 to 20,000 nucleotides, transcription start site enrichment score > 4, and percent reads in peaks > 20%. We quantified the activity of each gene in the genome using the GeneActivity function in Signac[77], which sums the fragments in the gene body coordinates including 2 kb upstream region, according to Ensembl annotation EnsDb.Hsapiens.v86. For dimensionality reduction, we performed term frequency inverse document frequency (TF-IDF) normalization and singular value decomposition (SVD) on the peak-by-cell matrix. To visualize the dataset in 2-dimensions, we performed UMAP using the top 50 components and used graph-based clustering to find clusters. With a combination of known markers and label transfer from scRNA-seq data, we assigned cell labels to each snATAC-sequenced cell.

Transfer of scRNA-seq annotations: Given our fully annotated scRNA-seq object of cell types and subtypes of the 39 samples derived from the methods described above, we found anchors between the RNA object and the object of the 15 matching snATAC-seq samples. Label transfer was first performed at the cell-type level and performed a second time to label subtypes within each cell type-specific subset. First, gene activity scores derived above were compared to scRNA-seq gene expression counts via canonical correlation analysis (CCA) using the FindTransferAnchors function with the reduction parameter set to "cca" and the first 2000 variable features used from the scRNA-seq dataset. The resulting anchors found were used to predict cell type (or subtype) labels for each cell in the snATAC-seq dataset using the TransferData function, with the reference data parameter set to the scRNA-seq cell types or subtypes and weight reduction set to the latent semantic indexing (LSI) projection of the snATAC-seq data. Predicted labels were assigned to each cell and visualized

on the UMAP of the 15 snATAC-seq samples. For subtype label transfer, we repeated the data normalization and dimensionality reduction steps mentioned above for each subsetted cell type.

RNA and ATAC co-embedding for cDCs: After subsetting cDCs from both snATAC-seq and scRNA-seq datasets, we used FindIntegrationAnchors in Signac[77] to identify co-varying components of the snATAC-seq and scRNA-seq datasets. Then we leveraged CCA to co-embed cells from both the transcriptomic and epigenomic space using the identified canonical 'basis' vectors. The co-embedding in shared lower-dimensional space maximizes correlation between the two datasets, thus allowing joint analysis and cell-typing of scRNA-seq and snATAC-seq datasets. We re-assigned the snATAC-seq cells with cDC subpopulation labels from their mutual nearest scRNA-seq neighbors in the shared space, compared with the cell subtype label transfer results derived above, and decided on the final subtype labeling of snATAC cells based on consensus and marker gene activities.

Differential accessible region analysis for cDCs: DARs were identified in a similar fashion to DEGs. Using normalized values of the peaks of cDCs in our snATAC-seq data, DARs were found using FindMarkers, again comparing the identity classes of mregDC and cDC1 or mregDC and cDC2. Logistic regression was used to identify DARs, as it corrects for the sequencing depth by incorporating the total number of fragments as a latent variable. A log fold change threshold of 0.01 was used, with a minimum percentage of the same peaks detected in both classes set to 5% to increase sensitivity relative to DEG analysis because of the sparse nature of ATAC data. DARs were labeled with the closest gene to the region using the ClosestFeatures function in Seurat. DARs were selected using an unadjusted p-value of 0.01 due to a lack of signal using adjusted p-values. Thus, interpretations of DARs are not conclusive and merit further investigation and validation.

Global correlation, pathway and motif enrichment analyses for cDCs: To compute cell type similarities to migDCs, we first calculated the average peak accessibility for each cell type of each peak accessible in migDCs. Then, we calculated the pearson correlation of the average peak accessibility between the cell type and migDCs. To investigate cis-regulatory regions, we used the Genomic Regions Enrichment of Annotations Tool (GREAT)[69]. We input significantly upregulated and downregulated regions independently into GREAT, yielding GO biological processes. For processes identified to be enriched in both upregulated and downregulated regions of the same comparison, the processes were removed. Significant GO biological processes were visualized using clusterProfiler[78] and enrichplot[79]. To investigate differentially accessible motifs between cDCs, we added motif information using JASPAR2022 and BSgenome.Hsapiens.UCSC.hg38. Then, we computed the per-cell motif activity score using Signac's implementation of chromVAR. We used FindMarkers in the chromVAR assay to find the resulting differentially accessible motifs.

Integration with previous single-cell studies

Tirosh *et al*.[7], Jerby-Arnon *et al*.[8] and Sade-Feldman *et al*.[9] had gene count matrices given in transcripts per million (TPM). Zhang *et al*.[10] provided a raw count matrix. We assumed that merging log normalized TPM and raw count matrices would capture the differences in relative expression and the variation of gene expression would be preserved, which was proven to be true. As each count matrix in their available data format from each study was converted into a Seurat object, we performed integration feature selection with SelectIntegrationFeatures and anchor discovery using log normalization and canonical correlation analysis (CCA) reduction with FindIntegrationAnchors. After obtaining the set of anchors, we integrated the five objects using IntegrateData. For label transfer, another set of anchors were found from our study's object as the reference and applied to a subset of the integrated object corresponding to the four studies as the query using PCA reduction of the reference. Predicted cell types and subtypes of the scRNA-seq of the four studies were predicted in a similar fashion to the label transfer of cell types and subtypes from scRNA-seq to snATAC-seq as described above. Subtypes were found after the annotation of cell types. For the construction of the final UMAP of the integrated object of all studies, the default assay was set to "integrated" and then scaled using the function ScaleData. PCA was applied using the variable features of the integrated object, and RunUMAP was executed on the first 30 PCs of the PCA reduction. No further batch correction was needed as cells from different studies were well integrated and cell types were clearly separated on the UMAP embedding.

Identification of cell states and DEGs associated with mregDC proportions

Algorithm: When performing DEG analysis between samples, we aim to explore which cell state is associated with the mregDC groups and what DEGs characterize this cell state. Existing methods for detecting DEGs, such as pseudo-bulk and mixed models, assume homogeneous populations when comparing subtypes and

treating all cells from one sample equally. Hence, the analysis still operates at a sample level and does not leverage the between-cell heterogeneity available in the scRNA-seq data. Our assumption is that, instead of the whole cell population in a group, mregDC proportion affects certain binary cell states in a cell type, e.g., exhaustion, activation, apoptosis, etc, and we aim to extract the mregDC-associated cell states and identify the DEGs in these cell states. To address this, we performed the DEG analysis in two steps, 1) identify cell states associated with the mregDC groups, 2) identify DEGs for this cell state. In Step 1, we developed a factorization algorithm to find the binary variable that explains the most variability of the count matrix with the adjustment for the covariates and sample-level heterogeneity under a Negative Binomial mixed model as in NEBULA [80]. Conceptually similar to the top principle component, this identified binary variable is the major cell state of the cell type. Our algorithm also returned the uncertainty of the estimation of the cell state and this uncertainty was used in the following steps to conduct valid testing for DEGs. In Step2, we then performed an association test between the extracted cell state and the mregDC groups in each cell type or subtype to identify the mregDC-associated state using a logistic mixed model. For those mregDC-associated states, we obtained their DEGs using the Negative Binomial mixed model implemented in NEBULA[80] and further took into account the uncertainty in the cell state estimation. We predict that this algorithm would find the cell states that drove the difference observed between the mregDC high group and the mregDC low group if mregDC is the major underlying factor driving the differential expression and the DEGs would be the potential regulators of the mregDC phenotype, especially at the cell-type level.

Model building: The model takes in two pieces of data: first, the raw gene by count matrix of the samples, and second, the metadata associated with each sample, which is used as the design matrix. First, we compiled the raw count matrices of all samples, which were subsetted by cell type or cell subtype. Then we created the design matrix, which included the mregDC group variable, which was 0 for an mregDC low sample (mregDC/cDC ≤ 0.185) or 1 for an mregDC high sample (mregDC/cDC > 0.185). The design matrix also included the sample-level variables to account for. We selected the sample level variables of age, sex, tissue of biopsy (skin, lymph, other), treatment state (pre, on, post), and treatment group (other, with ICI, ICI only, anti-PD1) and the cell-level variables of mitochondrial gene percentage and ribosomal gene percentage. Sample or cell-level variables for which all cells in the subset had the same value were removed from the design matrix prior to running NEBULA. The offset was set to the number of counts of RNA, i.e., the total number of molecules detected within a cell. NEBULA[80] was first run for each cell type and subtype to estimate the overdispersions, in which the count matrix, offset term, and design matrix were inputs to the model. Then, given the overdispersions, a factorization algorithm for the top binary factor was run for each cell type. We used the factors called from this step as the major cell states for cell subtypes and tested its association with the mregDC group. For mregDC-associated cell states, we used NEBULA[80] again to obtain the DEGs associated with these states.

Pathway analysis for identified DEGs: We used the fGSEA (fast gene set enrichment analysis) package in R. We narrowed down the gene set of canonical pathways to test enrichment, which was downloaded from https://www.gsea-msigdb.org/gsea/msigdb/human/collections.jsp. The list of all genes (significant and not significant) with their associated log fold change values were used as input to fgsea, setting the pathways to the downloaded canonical pathway gene set and testing for positively and negatively enriched pathways (scoreType parameter = 'std' for standard). Given the output of pathways, we identified main pathways, which are pathways that are independent from each other, using the function collapsePathways and an adjusted p-value less than 0.05 using the Benjamini-Hochberg correction, which was the default. The top pathways with the highest enrichment scores and adjusted p-value < 0.05 were visualized using aPEAR (Advanced Pathway Enrichment Analysis Representation)[81], a separate package in R that can generate enrichment networks from pathways that are similar to each other. All the canonical pathways generated from the cell type or subtype subsets were used as input, together with their adjusted p-values, normalized enrichment score, the number of genes in the pathway, and the list of genes in the pathway. Using a similarity metric to cluster redundant

pathways, aPEAR assigns a general name for the clusters of pathways using the PageRank algorithm[81]. All default parameters were used in the clustering and visualization of the pathways.

Bulk RNA-seq meta-cohort data analysis

To determine whether or not a signature of mregDCs is able to stratify an independent cohort of 274 ICI-treated patients with metastatic melanoma and with RNA-seq data[28], we used ssGSEA to score the mregDC signature (387 genes positively define mregDCs, **Supplementary Table 3**) in the bulk RNA-seq data set, and then performed response comparisons and survival analysis the same as described in the scRNA-seq section.

Data availability

The original data are available at GEO (GSEXXXXXX). The processed data are available on Zenodo (URL).

Code availability

All codes that are necessary to reproduce all the results in the paper are implemented in Python and R and are publicly available at GitHub (https://github.com/KellisLab/scCancer).

Supplemental information

Supplementary Figure 1. A five-study metastatic melanoma single-cell atlas. We integrated our single-cell dataset with four published single-cell datasets (Tirosh *et al*., Jerby-Arnon *et al*., Sade-Feldman *et al*., and Zhang *et al*.). Uniform manifold approximation and projection (UMAP) embedding of all the cells from the five studies (n=352,966 cells), with each color representing a study (**A**), a cell type (**B**), and a sample (**C**). **D**, Distribution of cells by cell types across different studies. **E**, Dotplot showing average expression and percent expression of marker genes across all the cells from the five studies.

Supplementary Figure 2. Cell subtype proportion correlations for subset or additional samples. A,C, Heatmap illustrating correlation coefficients among the relative proportions of cell subtypes in relation to their corresponding cell types across samples treated with ICI (**A**), or samples from the five studies (**C**). We identified clusters/modules by segmenting the hierarchical clustering tree at the red line and assigned annotations based on the modules discovered in **Fig. 2F**. **B**, UMAP embedding of all the cells from the five studies, with each color representing a subtype as annotated in this study.

Supplementary Figure 3. Cell subtype association with treatment response and patient survival. A-D, Boxplots comparing relative proportions of selected cell subtypes (**A**), cDC1 and cDC2 (**B**), and mregDC (**C**), and proportions of cDC out of all cells or immune cells (**D**) between non-responders and responders for all samples. Each dot represents a sample, with its color corresponding to the treatment group and its shape corresponding to the melanoma subtype. **E-F**, Survival plots for ICI-only samples split by selected subtype relative proportions (**E**) or samples treated with ICI and all samples split by TCF7+ CD8 T cell ratio (**F**). P values for boxplots were calculated using the Wilcoxon Rank Sum test. P values for survival plots were calculated using the Log Rank Sum test. NR, non-responder; R, responder; combo, anti-PD-1+anti-CTLA-4; PFS, progression free survival; OS, overall survival.

Supplementary Figure 4. Expression patterns of markers reported in other studies and additional cell-cell communication across cDC subtypes. A, Heatmap plotting expressions of marker genes reported in Maier *et al*. in mregDC, cDC1 and cDC2. **B**, Dotplots showing expression patterns of genes grouped by biological processes, as reported in Maier *et al*., across cDC subtypes. **C**, Heatmap illustrating average expression of genes for cDC1, cDC2 and mregDC. Gene groups were obtained from Broz *et al*. **D,E**, Dotplots illustrating inferred cell-cell communications either with differential activities between mregDC and other cDC or exclusively detected in mregDC, with cDC expressing ligands (**D**) or receptors (**E**) and monocyte/macrophage subtypes expressing receptors (**D**) or ligands (**E**), respectively. P values for dotplots were calculated using the Wilcoxon Rank Sum test.

Supplementary Figure 5. Cell-cell communications with differential activities associated with mregDC proportions. A,B, Networks depicting cell-cell interactions, inferred by using CellPhoneDB[41], with differential activities (co-expression patterns) in mregDC high samples vs. mregDC low samples. Nodes represent cell types (**A**) or subtypes (**B**). Node sizes correspond to the number of cells in the cell type/subtype within the cohort (mregDC high or low). Edge weights are equal to the number of interactions between each pair of cell types/subtypes.

Supplementary Table 1. Sample demographics and quality control measures. See Fig. 1 and Extended Data Fig. 1.

Supplementary Table 2. Cell type markers in reference to all the other cells. See Fig. 1.

Supplementary Table 3. Non-tumor cell subtype markers in reference to all the other cells. See Fig. 2 and Extended Data Fig. 2.

Supplementary Table 4. Tumor program markers in reference to the other tumor programs. See Fig. 2.

Supplementary Table 5. Abundance of cell types and subtypes and subtype proportions at the sample level. See Fig. 2,3, Extended Data Fig. 2,3, and Supplementary Fig. 2,3.

Supplementary Table 6. Differentially expressed genes between mregDC and other cDCs. See Fig. 4.

Supplementary Table 7. Pathways enriched in differentially expressed genes between mregDC and other cDCs. See Fig. 4.

Supplementary Table 8. Inferred cell-cell communication with differential activities or exclusively detected in mregDC compared to other cDCs with cDC as source. See Fig. 4, Extended Data Fig. 4, and Supplementary Fig. 4.

Supplementary Table 9. Inferred cell-cell communication with differential activities or exclusively detected in mregDC compared to other cDCs with cDC as target. See Fig. 4, Extended Data Fig. 4, and Supplementary Fig. 4.

Supplementary Table 10. Differentially accessible regions between mregDC and other cDCs. See Fig. 5 and Extended Data Fig. 5.

Supplementary Table 11. Motifs enriched in differentially accessible regions between mregDC and other cDCs. See Fig. 5 and Extended Data Fig. 5.

Supplementary Table 12. Cell type-specific differentially expressed genes between mregDC high and low samples. See Fig. 6.

Supplementary Table 13. Cell subtype-specific differentially expressed genes between mregDC high and low samples. See Extended Fig. 6.

Supplementary Table 14. Cell-cell communications showing differential activities between mregDC high and low samples. See Supplementary Fig. 5.

References

1. Liu W, Puri A, Fu D, Chen L, Wang C, Kellis M, Yang J. Dissecting the tumor microenvironment in response to immune checkpoint inhibitors via single-cell and spatial transcriptomics. Clin Exp Metastasis [Internet]. 2023 Dec 8; Available from: http://dx.doi.org/10.1007/s10585-023-10246-2 PMID: 38064127

2. Knight A, Karapetyan L, Kirkwood JM. Immunotherapy in Melanoma: Recent Advances and Future Directions. Cancers [Internet]. 2023 Feb 9;15(4). Available from: http://dx.doi.org/10.3390/cancers15041106 PMCID: PMC9954703

3. Larkin J, Chiarion-Sileni V, Gonzalez R, Grob JJ, Rutkowski P, Lao CD, Cowey CL, Schadendorf D, Wagstaff J, Dummer R, Ferrucci PF, Smylie M, Hogg D, Hill A, Márquez-Rodas I, Haanen J, Guidoboni M, Maio M, Schöffski P, Carlino MS, Lebbé C, McArthur G, Ascierto PA, Daniels GA, Long GV, Bastholt L, Rizzo JI, Balogh A, Moshyk A, Hodi FS, Wolchok JD. Five-Year Survival with Combined Nivolumab and Ipilimumab in Advanced Melanoma. N Engl J Med. 2019 Oct 17;381(16):1535–1546. PMID: 31562797

4. Rohaan MW, Borch TH, van den Berg JH, Met Ö, Kessels R, Geukes Foppen MH, Stoltenborg Granhøj J, Nuijen B, Nijenhuis C, Jedema I, van Zon M, Scheij S, Beijnen JH, Hansen M, Voermans C, Noringriis IM, Monberg TJ, Holmstroem RB, Wever LDV, van Dijk M, Grijpink-Ongering LG, Valkenet LHM, Torres Acosta A, Karger M, Borgers JSW, Ten Ham RMT, Retèl VP, van Harten WH, Lalezari F, van Tinteren H, van der Veldt AAM, Hospers GAP, Stevense-den Boer MAM, Suijkerbuijk KPM, Aarts MJB, Piersma D, van den Eertwegh AJM, de Groot JWB, Vreugdenhil G, Kapiteijn E, Boers-Sonderen MJ, Fiets WE, van den Berkmortel FWPJ, Ellebaek E, Hölmich LR, van Akkooi ACJ, van Houdt WJ, Wouters MWJM, van Thienen JV, Blank CU, Meerveld-Eggink A, Klobuch S, Wilgenhof S, Schumacher TN, Donia M, Svane IM, Haanen JBAG. Tumor-Infiltrating Lymphocyte Therapy or Ipilimumab in Advanced Melanoma. N Engl J Med. 2022 Dec 8;387(23):2113–2125. PMID: 36477031

5. Van Allen EM, Miao D, Schilling B, Shukla SA, Blank C, Zimmer L, Sucker A, Hillen U, Foppen MHG, Goldinger SM, Utikal J, Hassel JC, Weide B, Kaehler KC, Loquai C, Mohr P, Gutzmer R, Dummer R, Gabriel S, Wu CJ, Schadendorf D, Garraway LA. Genomic correlates of response to CTLA-4 blockade in metastatic melanoma. Science. 2015 Oct 9;350(6257):207–211. PMCID: PMC5054517

6. Tumeh PC, Yearley JH, Shintaku IP, Taylor EJM, Robert L, Chmielowski B, Spasic M, Henry G, Ciobanu V, West AN, Carmona M, Kivork C, Seja E, Cherry G, Gutierrez AJ, Grogan TR, Mateus C, Tomasic G, Glaspy JA, Emerson RO, Robins H, Pierce RH, Elashoff DA, Robert C, Ribas A. PD-1 blockade induces responses by inhibiting adaptive immune resistance. Nature. Nature Publishing Group; 2014 Nov 26;515(7528):568–571.

7. Tirosh I, Izar B, Prakadan SM, Wadsworth MH 2nd, Treacy D, Trombetta JJ, Rotem A, Rodman C, Lian C, Murphy G, Fallahi-Sichani M, Dutton-Regester K, Lin JR, Cohen O, Shah P, Lu D, Genshaft AS, Hughes TK, Ziegler CGK, Kazer SW, Gaillard A, Kolb KE, Villani AC, Johannessen CM, Andreev AY, Van Allen EM, Bertagnolli M, Sorger PK, Sullivan RJ, Flaherty KT, Frederick DT, Jané-Valbuena J, Yoon CH, Rozenblatt-Rosen O, Shalek AK, Regev A, Garraway LA. Dissecting the multicellular ecosystem of metastatic melanoma by single-cell RNA-seq. Science. 2016 Apr 8;352(6282):189–196. PMCID: PMC4944528

8. A Cancer Cell Program Promotes T Cell Exclusion and Resistance to Checkpoint Blockade. Cell. Cell Press; 2018 Nov 1;175(4):984–997.e24.

9. Sade-Feldman M, Yizhak K, Bjorgaard SL, Ray JP, de Boer CG, Jenkins RW, Lieb DJ, Chen JH, Frederick DT, Barzily-Rokni M, Freeman SS, Reuben A, Hoover PJ, Villani AC, Ivanova E, Portell A, Lizotte PH, Aref AR, Eliane JP, Hammond MR, Vitzthum H, Blackmon SM, Li B, Gopalakrishnan V, Reddy SM, Cooper ZA, Paweletz CP, Barbie DA, Stemmer-Rachamimov A, Flaherty KT, Wargo JA, Boland GM, Sullivan RJ, Getz G, Hacohen N. Defining T Cell States Associated with Response to Checkpoint Immunotherapy in Melanoma. Cell. 2019 Jan 10;176(1-2):404. PMCID: PMC6647017

10. Zhang C, Shen H, Yang T, Li T, Liu X, Wang J, Liao Z, Wei J, Lu J, Liu H, Xiang L, Yang Y, Yang M, Wang D, Li Y, Xing R, Teng S, Zhao J, Yang Y, Zhao G, Chen K, Li X, Yang J. A single-cell analysis reveals tumor heterogeneity and immune environment of acral melanoma. Nat Commun. 2022 Nov 25;13(1):7250. PMCID: PMC9700682

11. Steinman RM, Cohn ZA. Identification of a novel cell type in peripheral lymphoid organs of mice. I. Morphology, quantitation, tissue distribution. J Exp Med. 1973 May 1;137(5):1142–1162. PMCID: PMC2139237

12. Kvedaraite E, Ginhoux F. Human dendritic cells in cancer. Science Immunology [Internet]. American Association for the Advancement of Science; 2022 Apr 1 [cited 2024 Apr 17]; Available from: https://www.science.org/doi/10.1126/sciimmunol.abm9409

13. Murphy TL, Murphy KM. Dendritic cells in cancer immunology. Cell Mol Immunol. Nature Publishing Group; 2021 Sep 3;19(1):3–13.

14. Wang C, Chen L, Fu D, Liu W, Puri A, Kellis M, Yang J. Antigen presenting cells in cancer immunity and mediation of immune checkpoint blockade. Clin Exp Metastasis. Springer; 2024 Jan 23;1–17.

15. Mellman I, Steinman RM. Dendritic cells: specialized and regulated antigen processing machines. Cell. 2001 Aug 10;106(3):255–258. PMID: 11509172

16. Maier B, Leader AM, Chen ST, Tung N, Chang C, LeBerichel J, Chudnovskiy A, Maskey S, Walker L, Finnigan JP, Kirkling ME, Reizis B, Ghosh S, D'Amore NR, Bhardwaj N, Rothlin CV, Wolf A, Flores R, Marron T, Rahman AH, Kenigsberg E, Brown BD, Merad M. A conserved dendritic-cell regulatory program limits antitumour immunity. Nature. 2020 Apr;580(7802):257–262. PMCID: PMC7787191

17. Ladányi A, Kiss J, Somlai B, Gilde K, Fejos Z, Mohos A, Gaudi I, Tímár J. Density of DC-LAMP(+) mature dendritic cells in combination with activated T lymphocytes infiltrating primary cutaneous melanoma is a strong independent prognostic factor. Cancer Immunol Immunother. 2007 Sep;56(9):1459–1469. PMCID: PMC11030123

18. Gavish A, Tyler M, Greenwald AC, Hoefflin R, Simkin D, Tschernichovsky R, Galili Darnell N, Somech E, Barbolin C, Antman T, Kovarsky D, Barrett T, Gonzalez Castro LN, Halder D, Chanoch-Myers R, Laffy J, Mints M, Wider A, Tal R, Spitzer A, Hara T, Raitses-Gurevich M, Stossel C, Golan T, Tirosh A, Suvà ML, Puram SV, Tirosh I. Hallmarks of transcriptional intratumour heterogeneity across a thousand tumours. Nature. 2023 Jun;618(7965):598–606. PMID: 37258682

19. Zhou Y, Zhu Y, Xie Y, Ma X. The Role of Long Non-coding RNAs in Immunotherapy Resistance. Front Oncol. 2019 Nov 28;9:1292. PMCID: PMC6892777

20. Hu ZW, Chen L, Ma RQ, Wei FQ, Wen YH, Zeng XL, Sun W, Wen WP. Comprehensive analysis of ferritin subunits expression and positive correlations with tumor-associated macrophages and T regulatory cells infiltration in most solid tumors. Aging . 2021 Apr 16;13(8):11491–11506. PMCID: PMC8109065

21. Araki K, Morita M, Bederman AG, Konieczny BT, Kissick HT, Sonenberg N, Ahmed R. Translation is actively regulated during the differentiation of CD8+ effector T cells. Nat Immunol. Nature Publishing Group; 2017 Jul 17;18(9):1046–1057.

22. Wu Z, Zheng Y, Sheng J, Han Y, Yang Y, Pan H, Yao J. CD3CD4CD8 (Double-Negative) T Cells in Inflammation, Immune Disorders and Cancer. Front Immunol. 2022 Feb 10;13:816005. PMCID: PMC8866817

23. Peranzoni E, Ingangi V, Masetto E, Pinton L, Marigo I. Myeloid Cells as Clinical Biomarkers for Immune Checkpoint Blockade. Front Immunol. 2020 Jul 24;11:1590. PMCID: PMC7393010

24. Zilionis R, Engblom C, Pfirschke C, Savova V, Zemmour D, Saatcioglu HD, Krishnan I, Maroni G, Meyerovitz CV, Kerwin CM, Choi S, Richards WG, De Rienzo A, Tenen DG, Bueno R, Levantini E, Pittet MJ, Klein AM. Single-Cell Transcriptomics of Human and Mouse Lung Cancers Reveals Conserved Myeloid Populations across Individuals and Species. Immunity. 2019 May 21;50(5):1317–1334.e10. PMCID: PMC6620049

25. Zhang Q, He Y, Luo N, Patel SJ, Han Y, Gao R, Modak M, Carotta S, Haslinger C, Kind D, Peet GW, Zhong G, Lu S, Zhu W, Mao Y, Xiao M, Bergmann M, Hu X, Kerkar SP, Vogt AB, Pflanz S, Liu K, Peng J, Ren X, Zhang Z. Landscape and Dynamics of Single Immune Cells in Hepatocellular Carcinoma. Cell. 2019 Oct 31;179(4):829–845.e20. PMID: 31675496

26. Bassez A, Vos H, Van Dyck L, Floris G, Arijs I, Desmedt C, Boeckx B, Vanden Bempt M, Nevelsteen I, Lambein K, Punie K, Neven P, Garg AD, Wildiers H, Qian J, Smeets A, Lambrechts D. A single-cell map of intratumoral changes during anti-PD1 treatment of patients with breast cancer. Nat Med. 2021 May;27(5):820–832. PMID: 33958794

27. Peng Q, Qiu X, Zhang Z, Zhang S, Zhang Y, Liang Y, Guo J, Peng H, Chen M, Fu YX, Tang H. PD-L1 on dendritic cells attenuates T cell activation and regulates response to immune checkpoint blockade. Nat Commun. 2020 Sep 24;11(1):4835. PMCID: PMC7518441

28. Huang AY, Burke KP, Porter R, Fatouros P, Vokes N, Ricker C, Robitschek E, Tarantino G, Aprati TJ, Glettig MC, Chen J, He Y, Yang J, Ho LL, Galani K, Freeman G, Van Allen EM, Kellis M, Boland GM, Sharpe AH, Liu D. Stratified analysis identifies hypoxia as a therapeutic target for immune-high melanomas.

29. Murphy TL, Grajales-Reyes GE, Wu X, Tussiwand R, Briseño CG, Iwata A, Kretzer NM, Durai V, Murphy KM. Transcriptional Control of Dendritic Cell Development. Annu Rev Immunol. 2016 May 20;34:93–119.

PMCID: PMC5135011

30. Broz ML, Binnewies M, Boldajipour B, Nelson AE, Pollack JL, Erle DJ, Barczak A, Rosenblum MD, Daud A, Barber DL, Amigorena S, Van't Veer LJ, Sperling AI, Wolf DM, Krummel MF. Dissecting the tumor myeloid compartment reveals rare activating antigen-presenting cells critical for T cell immunity. Cancer Cell. 2014 Nov 10;26(5):638–652. PMCID: PMC4254577

31. Gulati GS, Sikandar SS, Wesche DJ, Manjunath A, Bharadwaj A, Berger MJ, Ilagan F, Kuo AH, Hsieh RW, Cai S, Zabala M, Scheeren FA, Lobo NA, Qian D, Yu FB, Dirbas FM, Clarke MF, Newman AM. Single-cell transcriptional diversity is a hallmark of developmental potential. Science. 2020 Jan 24;367(6476):405–411. PMCID: PMC7694873

32. Aibar S, González-Blas CB, Moerman T, Huynh-Thu VA, Imrichova H, Hulselmans G, Rambow F, Marine JC, Geurts P, Aerts J, van den Oord J, Atak ZK, Wouters J, Aerts S. SCENIC: single-cell regulatory network inference and clustering. Nat Methods. 2017 Nov 1;14(11):1083–1086. PMCID: pmc5937676

33. Cui A, Huang T, Li S, Ma A, Pérez JL, Sander C, Keskin DB, Wu CJ, Fraenkel E, Hacohen N. Dictionary of immune responses to cytokines at single-cell resolution. Nature. 2024 Jan;625(7994):377–384. PMCID: PMC10781646

34. Ghislat G, Cheema AS, Baudoin E, Verthuy C, Ballester PJ, Crozat K, Attaf N, Dong C, Milpied P, Malissen B, Auphan-Anezin N, Manh TPV, Dalod M, Lawrence T. NF-κB-dependent IRF1 activation programs cDC1 dendritic cells to drive antitumor immunity. Sci Immunol [Internet]. 2021 Jul 9;6(61). Available from: http://dx.doi.org/10.1126/sciimmunol.abg3570 PMID: 34244313

35. Cytlak U, Resteu A, Bogaert D, Kuehn HS, Altmann T, Gennery A, Jackson G, Kumanovics A, Voelkerding KV, Prader S, Dullaers M, Reichenbach J, Hill H, Haerynck F, Rosenzweig SD, Collin M, Bigley V. Ikaros family zinc finger 1 regulates dendritic cell development and function in humans. Nat Commun. 2018 Mar 27;9(1):1239. PMCID: PMC5869589

36. Tussiwand R, Everts B, Grajales-Reyes GE, Kretzer NM, Iwata A, Bagaitkar J, Wu X, Wong R, Anderson DA, Murphy TL, Pearce EJ, Murphy KM. Klf4 expression in conventional dendritic cells is required for T helper 2 cell responses. Immunity. 2015 May 19;42(5):916–928. PMCID: PMC4447135

37. van de Laar L, Coffer PJ, Woltman AM. Regulation of dendritic cell development by GM-CSF: molecular control and implications for immune homeostasis and therapy. Blood. American Society of Hematology; 2012 Apr 12;119(15):3383–3393.

38. Liu YJ. TSLP in epithelial cell and dendritic cell cross talk. Adv Immunol. 2009;101:1–25. PMCID: PMC3645262

39. Bhardwaj N, Friedlander PA, Pavlick AC, Ernstoff MS, Gastman BR, Hanks BA, Curti BD, Albertini MR, Luke JJ, Blazquez AB, Balan S, Bedognetti D, Beechem JM, Crocker AS, D'Amico L, Danaher P, Davis TA, Hawthorne T, Hess BW, Keler T, Lundgren L, Morishima C, Ramchurren N, Rinchai D, Salazar AM, Salim BA, Sharon E, Vitale LA, Wang E, Warren S, Yellin MJ, Disis ML, Cheever MA, Fling SP. Flt3 ligand augments immune responses to anti-DEC-205-NY-ESO-1 vaccine through expansion of dendritic cell subsets. Nature Cancer. Nature Publishing Group; 2020 Nov 16;1(12):1204–1217.

40. Brandt K, Bulfone-Paus S, Foster DC, Rückert R. Interleukin-21 inhibits dendritic cell activation and maturation. Blood. 2003 Dec 1;102(12):4090–4098. PMID: 12893770

41. Efremova M, Vento-Tormo M, Teichmann SA, Vento-Tormo R. CellPhoneDB: inferring cell–cell communication from combined expression of multi-subunit ligand–receptor complexes. Nat Protoc. Nature Publishing Group; 2020 Feb 26;15(4):1484–1506.

42. Kalinski P. Regulation of immune responses by prostaglandin E2. J Immunol. 2012 Jan 1;188(1):21–28.

PMCID: PMC3249979

43. Pachynski RK, Wang P, Salazar N, Zheng Y, Nease L, Rosalez J, Leong WI, Virdi G, Rennier K, Shin WJ, Nguyen V, Butcher EC, Zabel BA. Chemerin Suppresses Breast Cancer Growth by Recruiting Immune Effector Cells Into the Tumor Microenvironment. Front Immunol. 2019 May 8;10:983. PMCID: PMC6518384

44. Choi BK, Kim YH, Kwon PM, Lee SC, Kang SW, Kim MS, Lee MJ, Kwon BS. 4-1BB functions as a survival factor in dendritic cells. J Immunol. 2009 Apr 1;182(7):4107–4115. PMCID: PMC2681223

45. Luan F, Li X, Cheng X, Huangfu L, Han J, Guo T, Du H, Wen X, Ji J. TNFRSF11B activates Wnt/β-catenin signaling and promotes gastric cancer progression. Int J Biol Sci. 2020 Apr 25;16(11):1956–1971. PMCID: PMC7211174

46. TWEAK Attenuates the Transition from Innate to Adaptive Immunity. Cell. Cell Press; 2005 Dec 2;123(5):931–944.

47. Schellenburg S, Schulz A, Poitz DM, Muders MH. Role of neuropilin-2 in the immune system. Mol Immunol. 2017 Oct;90:239–244. PMID: 28843905

48. Hafemeister C, Satija R. Normalization and variance stabilization of single-cell RNA-seq data using regularized negative binomial regression. Genome Biol. 2019 Dec 23;20(1):296. PMCID: PMC6927181

49. Zhou Q, Zhang Y, Wang B, Zhou W, Bi Y, Huai W, Chen X, Chen Y, Liu Z, Liu X, Zhan Z. KDM2B promotes IL-6 production and inflammatory responses through Brg1-mediated chromatin remodeling. Cell Mol Immunol. 2020 Aug;17(8):834–842. PMCID: PMC7395766

50. Yang R, Cheng S, Xiao J, Pei Y, Zhu Z, Zhang J, Feng J, Li J. GLS and GOT2 as prognostic biomarkers associated with dendritic cell and immunotherapy response in breast cancer. Heliyon. 2024 Jan 15;10(1):e24163. PMCID: PMC10792574

51. Devosse T, Dutoit R, Migeotte I, De Nadai P, Imbault V, Communi D, Salmon I, Parmentier M. Processing of HEBP1 by Cathepsin D Gives Rise to F2L, the Agonist of Formyl Peptide Receptor 3. J Immunol. American Association of Immunologists; 2011 Aug 1;187(3):1475–1485.

52. Yang D, Chen Q, Gertz B, He R, Phulsuksombati M, Ye RD, Oppenheim JJ. Human dendritic cells express functional formyl peptide receptor-like-2 (FPRL2) throughout maturation. J Leukoc Biol. Oxford Academic; 2002 Sep 1;72(3):598–607.

53. Kohyama M, Matsuoka S, Shida K, Sugihara F, Aoshi T, Kishida K, Ishii KJ, Arase H. Monocyte infiltration into obese and fibrilized tissues is regulated by PILRα. Eur J Immunol. John Wiley & Sons, Ltd; 2016 May 1;46(5):1214–1223.

54. O'Neill AF, Nguyen EM, Maldonado ED, Chang MR, Sun J, Zhu Q, Marasco WA. Anti-CD99 Antibody Therapy Triggers Macrophage-Dependent Ewing Cell Death In Vitro and Myeloid Cell Recruitment In Vivo. Antibodies. Multidisciplinary Digital Publishing Institute; 2024 Mar 18;13(1):24.

55. Baiula M, Spampinato S, Gentilucci L, Tolomelli A. Novel Ligands Targeting α4β1 Integrin: Therapeutic Applications and Perspectives. Front Chem. Frontiers; 2019 Jul 9;7:472116.

56. Spenlé C, Loustau T, Murdamoothoo D, Erne W, Beghelli-de la Forest Divonne S, Veber R, Petti L, Bourdely P, Mörgelin M, Brauchle EM, Cremel G, Randrianarisoa V, Camara A, Rekima S, Schaub S, Nouhen K, Imhof T, Hansen U, Paul N, Carapito R, Pythoud N, Hirschler A, Carapito C, Dumortier H, Mueller CG, Koch M, Schenke-Layland K, Kon S, Sudaka A, Anjuère F, Van Obberghen-Schilling E, Orend G. Tenascin-C Orchestrates an Immune-Suppressive Tumor Microenvironment in Oral Squamous Cell Carcinoma. Cancer Immunol Res. 2020 Sep;8(9):1122–1138. PMID: 32665262

57. Hendriks J, Gravestein LA, Tesselaar K, van Lier RAW, Schumacher TNM, Borst J. CD27 is required for generation and long-term maintenance of T cell immunity. Nat Immunol. Nature Publishing Group; 2000 Nov;1(5):433–440.

58. Hashimoto-Okada M, Kitawaki T, Kadowaki N, Iwata S, Morimoto C, Hori T, Uchiyama T. The CD70-CD27 interaction during the stimulation with dendritic cells promotes naive CD4(+) T cells to develop into T cells producing a broad array of immunostimulatory cytokines in humans. Int Immunol. 2009 Aug;21(8):891–904. PMID: 19556308

59. Signaling via a CD27-TRAF2-SHP-1 axis during naive T cell activation promotes memory-associated gene regulatory networks. Immunity. Cell Press; 2024 Feb 13;57(2):287–302.e12.

60. Kuang Y, Weng X, Liu X, Zhu H, Chen Z, Chen H. Effects of 4-1BB signaling on the biological function of murine dendritic cells. Oncol Lett. Spandidos Publications; 2012 Feb 1;3(2):477–481.

61. Muik A, Adams HC 3rd, Gieseke F, Altintas I, Schoedel KB, Blum JM, Sänger B, Burm SM, Stanganello E, Verzijl D, Spires VM, Vascotto F, Toker A, Quinkhardt J, Fereshteh M, Diken M, Satijn DPE, Kreiter S, Ahmadi T, Breij ECW, Türeci Ö, Sasser K, Sahin U, Jure-Kunkel M. DuoBody-CD40x4-1BB induces dendritic-cell maturation and enhances T-cell activation through conditional CD40 and 4-1BB agonist activity. J Immunother Cancer [Internet]. 2022 Jun;10(6). Available from: http://dx.doi.org/10.1136/jitc-2021-004322 PMCID: PMC9189854

62. Zhang X, Peng L, Luo Y, Zhang S, Pu Y, Chen Y, Guo W, Yao J, Shao M, Fan W, Cui Q, Xi Y, Sun Y, Niu X, Zhao X, Chen L, Wang Y, Liu Y, Yang X, Wang C, Zhong C, Tan W, Wang J, Wu C, Lin D. Dissecting esophageal squamous-cell carcinoma ecosystem by single-cell transcriptomic analysis. Nat Commun. 2021 Sep 6;12(1):5291. PMCID: PMC8421382

63. Zheng Y, Chen Z, Han Y, Han L, Zou X, Zhou B, Hu R, Hao J, Bai S, Xiao H, Li WV, Bueker A, Ma Y, Xie G, Yang J, Chen S, Li H, Cao J, Shen L. Immune suppressive landscape in the human esophageal squamous cell carcinoma microenvironment. Nat Commun. 2020 Dec 8;11(1):6268. PMCID: PMC7722722

64. Smalley I, Chen Z, Phadke M, Li J, Yu X, Wyatt C, Evernden B, Messina JL, Sarnaik A, Sondak VK, Zhang C, Law V, Tran N, Etame A, Macaulay RJB, Eroglu Z, Forsyth PA, Rodriguez PC, Chen YA, Smalley KSM. Single-Cell Characterization of the Immune Microenvironment of Melanoma Brain and Leptomeningeal Metastases. Clin Cancer Res. American Association for Cancer Research; 2021 Jul 15;27(14):4109–4125.

65. Lee CYC, Kennedy BC, Richoz N, Dean I, Tuong ZK, Gaspal F, Li Z, Willis C, Hasegawa T, Whiteside SK, Posner DA, Carlesso G, Hammond SA, Dovedi SJ, Roychoudhuri R, Withers DR, Clatworthy MR. Tumour-retained activated CCR7+ dendritic cells are heterogeneous and regulate local anti-tumour cytolytic activity. Nat Commun. Nature Publishing Group; 2024 Jan 24;15(1):1–18.

66. Chen JH, Nieman LT, Spurrell M, Jorgji V, Elmelech L, Richieri P, Xu KH, Madhu R, Parikh M, Zamora I, Mehta A, Nabel CS, Freeman SS, Pirl JD, Lu C, Meador CB, Barth JL, Sakhi M, Tang AL, Sarkizova S, Price C, Fernandez NF, Emanuel G, He J, Van Raay K, Reeves JW, Yizhak K, Hofree M, Shih A, Sade-Feldman M, Boland GM, Pelka K, Aryee MJ, Mino-Kenudson M, Gainor JF, Korsunsky I, Hacohen N. Human lung cancer harbors spatially organized stem-immunity hubs associated with response to immunotherapy. Nat Immunol. Nature Publishing Group; 2024 Mar 19;25(4):644–658.

67. Cheng S, Li Z, Gao R, Xing B, Gao Y, Yang Y, Qin S, Zhang L, Ouyang H, Du P, Jiang L, Zhang B, Yang Y, Wang X, Ren X, Bei JX, Hu X, Bu Z, Ji J, Zhang Z. A pan-cancer single-cell transcriptional atlas of tumor infiltrating myeloid cells. Cell. 2021 Feb 4;184(3):792–809.e23. PMID: 33545035

68. Brand U, Bellinghausen I, Enk AH, Jonuleit H, Becker D, Knop J, Saloga J. Influence of extracellular matrix proteins on the development of cultured human dendritic cells. Eur J Immunol. 1998

May;28(5):1673–1680. PMID: 9603474

69. McLean CY, Bristor D, Hiller M, Clarke SL, Schaar BT, Lowe CB, Wenger AM, Bejerano G. GREAT improves functional interpretation of cis-regulatory regions. Nat Biotechnol. 2010 May;28(5):495–501. PMCID: PMC4840234

70. Fleming SJ, Chaffin MD, Arduini A, Akkad AD, Banks E, Marioni JC, Philippakis AA, Ellinor PT, Babadi M. Unsupervised removal of systematic background noise from droplet-based single-cell experiments using CellBender. Nat Methods. 2023 Sep;20(9):1323–1335. PMID: 37550580

71. Wolock SL, Lopez R, Klein AM. Scrublet: Computational Identification of Cell Doublets in Single-Cell Transcriptomic Data. Cell Syst. 2019 Apr 24;8(4):281–291.e9. PMCID: PMC6625319

72. Integrated analysis of multimodal single-cell data. Cell. Cell Press; 2021 Jun 24;184(13):3573–3587.e29.

73. Korsunsky I, Millard N, Fan J, Slowikowski K, Zhang F, Wei K, Baglaenko Y, Brenner M, Loh PR, Raychaudhuri S. Fast, sensitive and accurate integration of single-cell data with Harmony. Nat Methods. 2019 Dec;16(12):1289–1296. PMCID: PMC6884693

74. Zhou Y, Zhou B, Pache L, Chang M, Khodabakhshi AH, Tanaseichuk O, Benner C, Chanda SK. Metascape provides a biologist-oriented resource for the analysis of systems-level datasets. Nat Commun. 2019 Apr 3;10(1):1523. PMCID: PMC6447622

75. Lange M, Bergen V, Klein M, Setty M, Reuter B, Bakhti M, Lickert H, Ansari M, Schniering J, Schiller HB, Pe'er D, Theis FJ. CellRank for directed single-cell fate mapping. Nat Methods. Nature Publishing Group; 2022 Jan 13;19(2):159–170.

76. Hie B, Cho H, DeMeo B, Bryson B, Berger B. Geometric Sketching Compactly Summarizes the Single-Cell Transcriptomic Landscape. Cell Syst. 2019 Jun 26;8(6):483–493.e7. PMCID: PMC6597305

77. Stuart T, Srivastava A, Madad S, Lareau CA, Satija R. Single-cell chromatin state analysis with Signac. Nat Methods. 2021 Nov;18(11):1333–1341. PMCID: PMC9255697

78. clusterProfiler 4.0: A universal enrichment tool for interpreting omics data. Innov J. Cell Press; 2021 Aug 28;2(3):100141.

79. Yu G. 📖 Introduction [Internet]. [cited 2024 May 3]. Available from: https://yulab-smu.top/biomedical-knowledge-mining-book/

80. He L, Kulminski AM. NEBULA: a fast negative binomial mixed model for differential expression and co-expression analyses of large-scale multi-subject single-cell data [Internet]. Cold Spring Harbor Laboratory. 2020 [cited 2021 Feb 8]. p. 2020.09.24.311662. Available from: https://www.biorxiv.org/content/10.1101/2020.09.24.311662v1

81. Kerseviciute I, Gordevicius J. aPEAR: an R package for autonomous visualization of pathway enrichment networks. Bioinformatics [Internet]. 2023 Nov 1;39(11). Available from: http://dx.doi.org/10.1093/bioinformatics/btad672 PMCID: PMC10641035

Figure 1

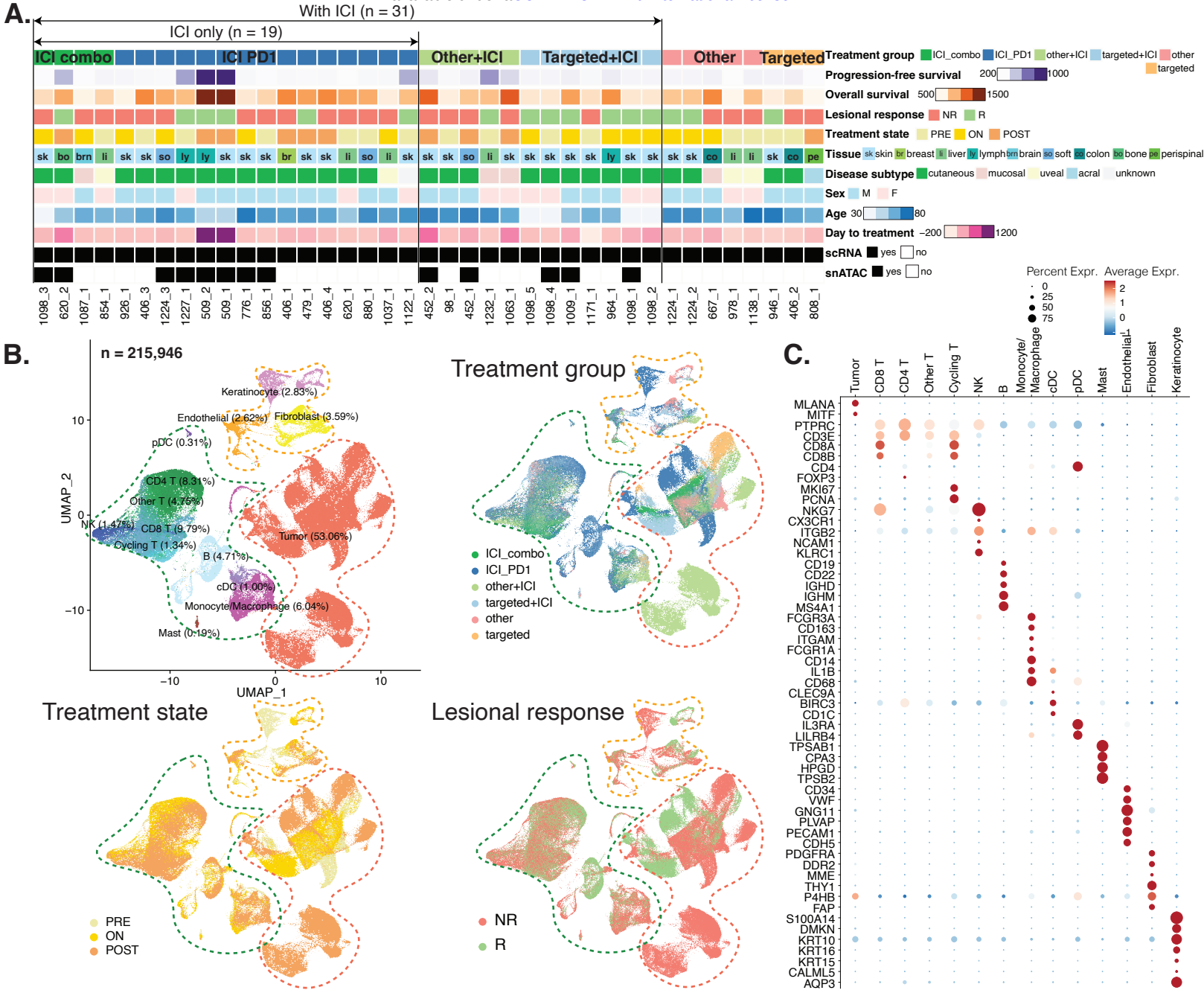

Figure 1. Characterization of cells in human metastatic melanoma tumors. A, Demographic summary of the 39 samples included in this study. Pfs, progression-free survival; os, overall survival; NR, non-responder; R, responder. **B,** Uniform manifold approximation and projection (UMAP) embedding of all the cells from the 39 samples, after quality control, with each color representing a cell type. **C,** Dotplot showing average normalized expression and percent normalized expression of marker genes across cell types.

Figure 2.

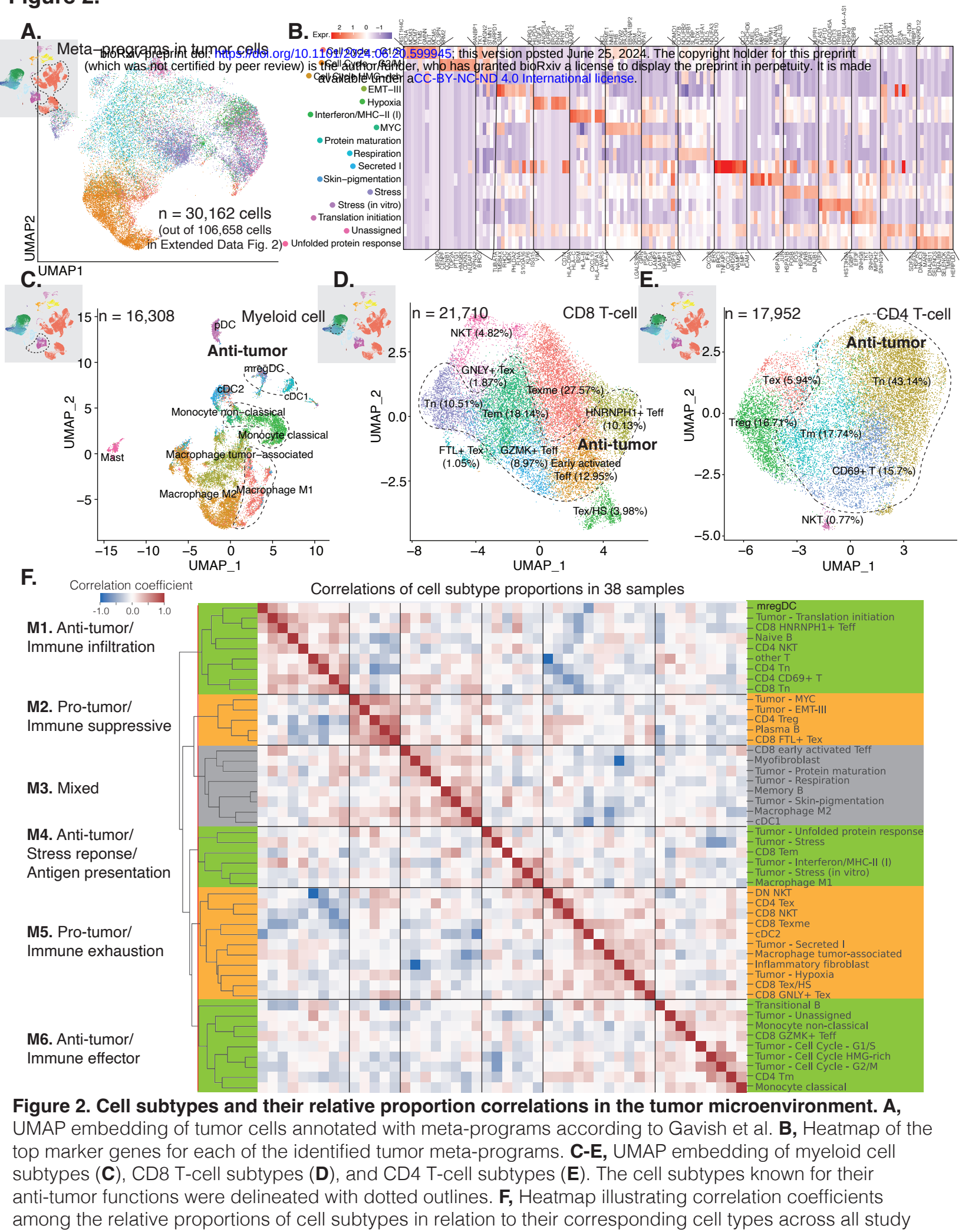

Figure 2. Cell subtypes and their relative proportion correlations in the tumor microenvironment. A, UMAP embedding of tumor cells annotated with meta-programs according to Gavish et al. **B,** Heatmap of the top marker genes for each of the identified tumor meta-programs. **C-E,** UMAP embedding of myeloid cell subtypes (**C**), CD8 T-cell subtypes (**D**), and CD4 T-cell subtypes (**E**). The cell subtypes known for their anti-tumor functions were delineated with dotted outlines. **F,** Heatmap illustrating correlation coefficients among the relative proportions of cell subtypes in relation to their corresponding cell types across all study samples. We identified clusters/modules by segmenting the hierarchical clustering tree at the red line and assigned annotations based on the known functions of the cell subtypes within each cluster or module.

Figure 3.

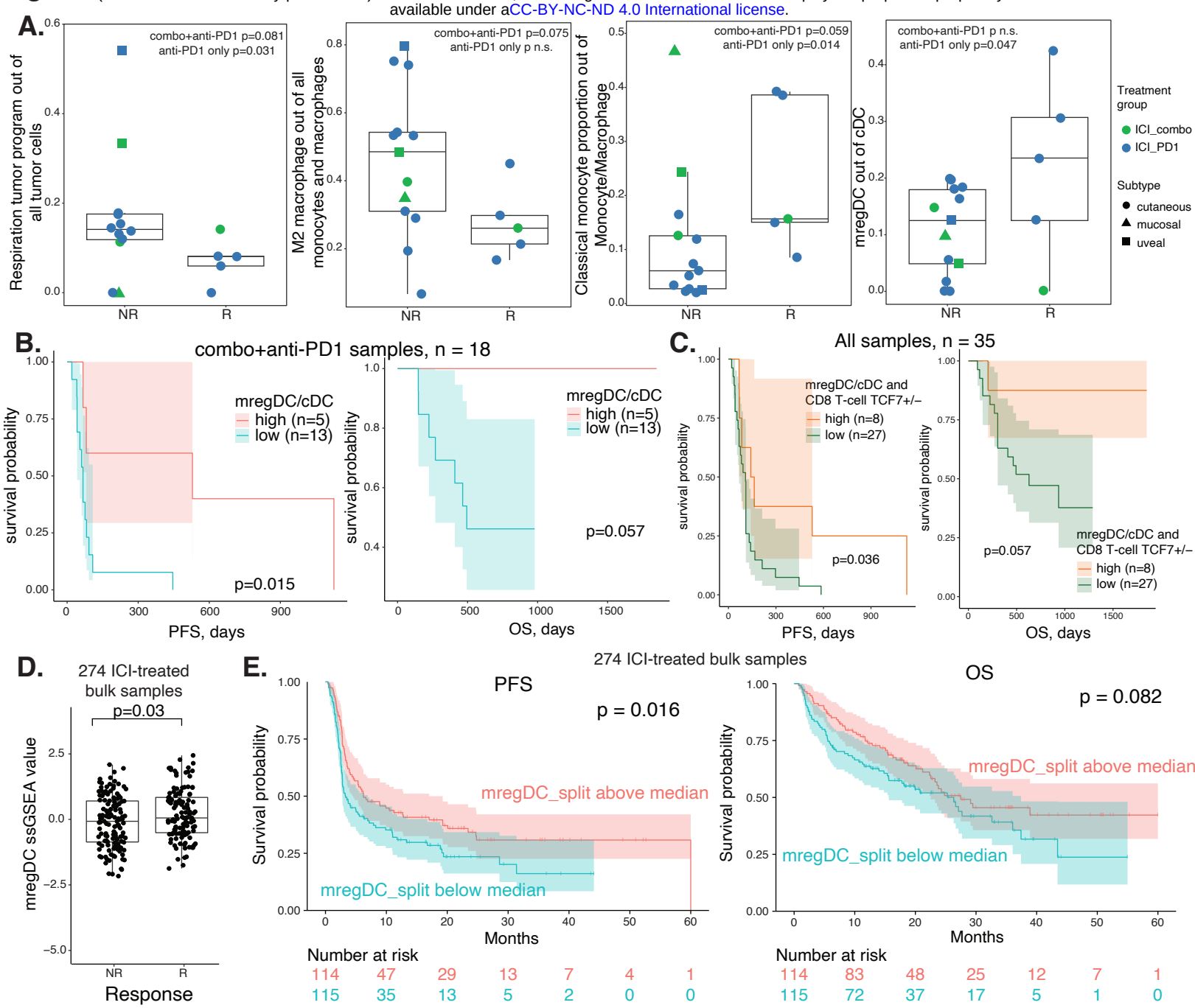

Figure 3. Mature and regulatory cDCs associated with ICI response and patient survival. A, Boxplots comparing relative proportions of four subtypes between ICI non-responders and responders. Each dot represents a sample, with its color corresponding to the type of ICI and its shape corresponding to the melanoma subtype. **B,** Survival plots for samples only treated with ICI and split by the median value of mregDC relative proportion. **C,** Survival plots for all samples and split by the median values of both mregDC relative proportion and TCF7+ CD8 T ratio. **D,** Boxplot comparing mregDC signature scores, calculated using ssGSEA, between non-responders and responders in 274 ICI-treated bulk RNA-seq samples. E, Survival plots for the 274 bulk RNA-seq samples split by the median value of their mregDC scores. P values for boxplots were calculated using the Wilcoxon Rank Sum test. P values for survival plots were calculated using the Log Rank Sum test. NR, non-responder; R, responder; combo, anti-PD-1+anti-CTLA-4; PFS, progression free survival; OS, overall survival.

Figure 4.

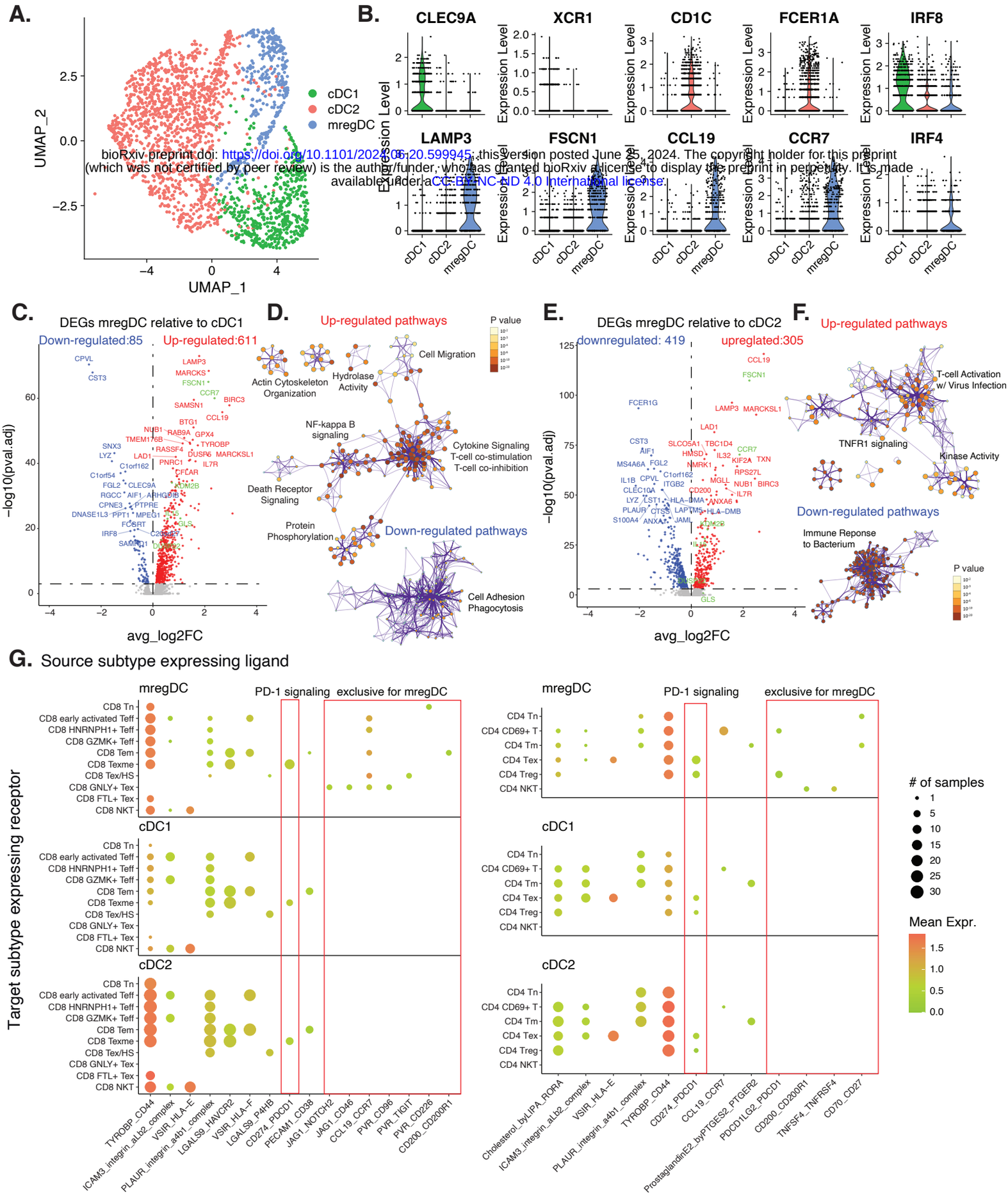

Figure 4. Transcriptional landscape and interactome of cDC subtypes. A, UMAP embedding of cDCs colored by the subtypes. **B,** Violin plots of canonical marker genes for cDC1, cDC2 and mregDC. **C,E,** Volcano plots showing differentially expressed genes (DEGs) between mregDC and cDC1 (**C**) and between mregDC and cDC2 (**E**). An adjusted P value of 0.001 was used to call significant DEGs. Examples of genes with mregDC-specific enhancers were colored in green, which were mentioned in Figure 5. **D,F,** Networks of enriched terms for DEGs up- or down-regulated in mregDC compared to cDC1 (**D**) or cDC2 (**F**). **G,** Dotplots illustrating inferred cell-cell communications by CellPhoneDB41 either with differential activities between mregDC and other cDC or exclusively detected in mregDC. The left and right panels plotted interactions with cDC expressing ligands and CD8 or CD4 T-cell expressing receptors, respectively. P values for volcano plots and dotplots were calculated using the Wilcoxon Rank Sum test.

Figure 5

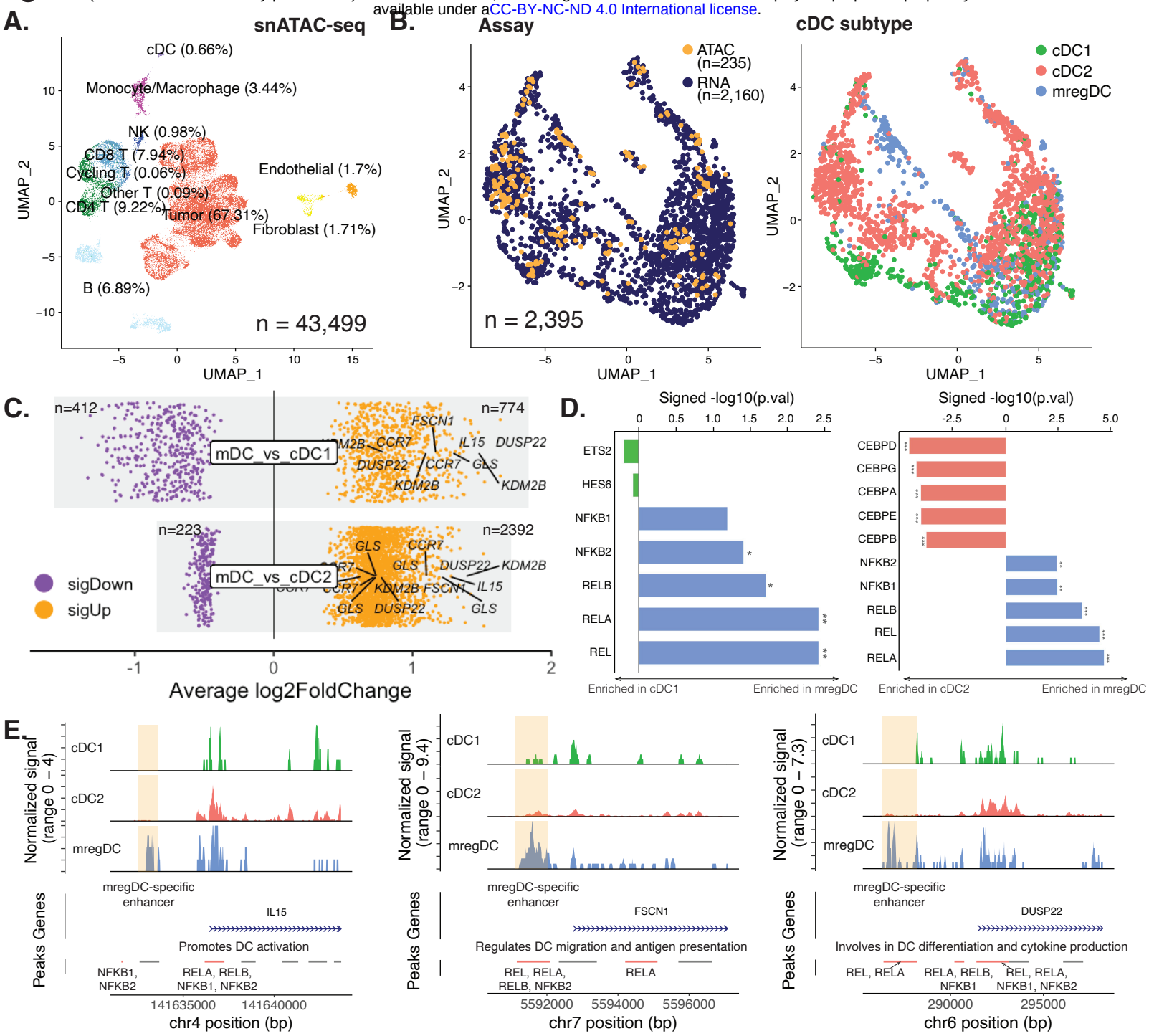

Figure 5. Epigenomic landscape of cDC subtypes using snATAC-seq data. A, UMAP embedding of snATAC-seq cells with cell type labels transferred from scRNA-seq data. **B,** Co-embedding of cDCs from scRNA-seq and snATAC-seq data, with colors corresponding to assays (left) or subtypes (right). **C,** Differentially accessible regions between mregDC and cDC1 (top), and mregDC and cDC2 (bottom). The p value cutoff is 0.01. **D,** Motifs enriched in differentially accessible regions between mregDC and cDC1 (left), and mregDC and cDC2 (right). Significantly enriched motifs were marked with an asterisk (adjusted p-value <=0.05). **E,** Track plots comparing normalized number of reads across cDC subtypes underlying enhancers associated with genes important for cDC functions. mDC is short for mregDC in some figure panels due to space constraints. A peak is colored orange if it contains motifs for members of the NF-κB transcription factor family.

Figure 6

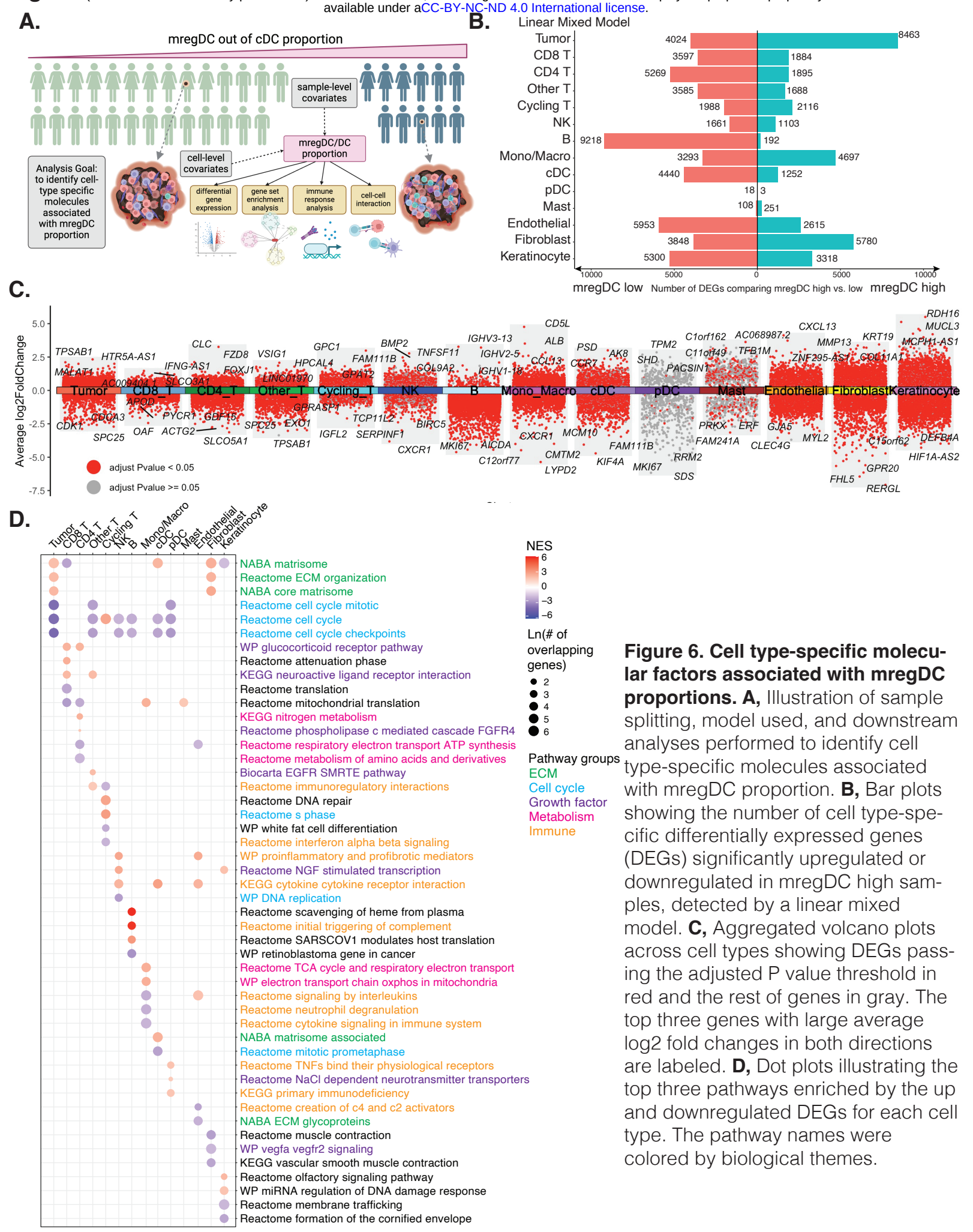

Figure 6. Cell type-specific molecular factors associated with mregDC proportions. A, Illustration of sample splitting, model used, and downstream analyses performed to identify cell type-specific molecules associated with mregDC proportion. **B,** Bar plots showing the number of cell type-specific differentially expressed genes (DEGs) significantly upregulated or downregulated in mregDC high samples, detected by a linear mixed model. **C,** Aggregated volcano plots across cell types showing DEGs passing the adjusted P value threshold in red and the rest of genes in gray. The top three genes with large average log2 fold changes in both directions are labeled. **D,** Dot plots illustrating the top three pathways enriched by the up and downregulated DEGs for each cell type. The pathway names were colored by biological themes.

Extended Data Figure 1.

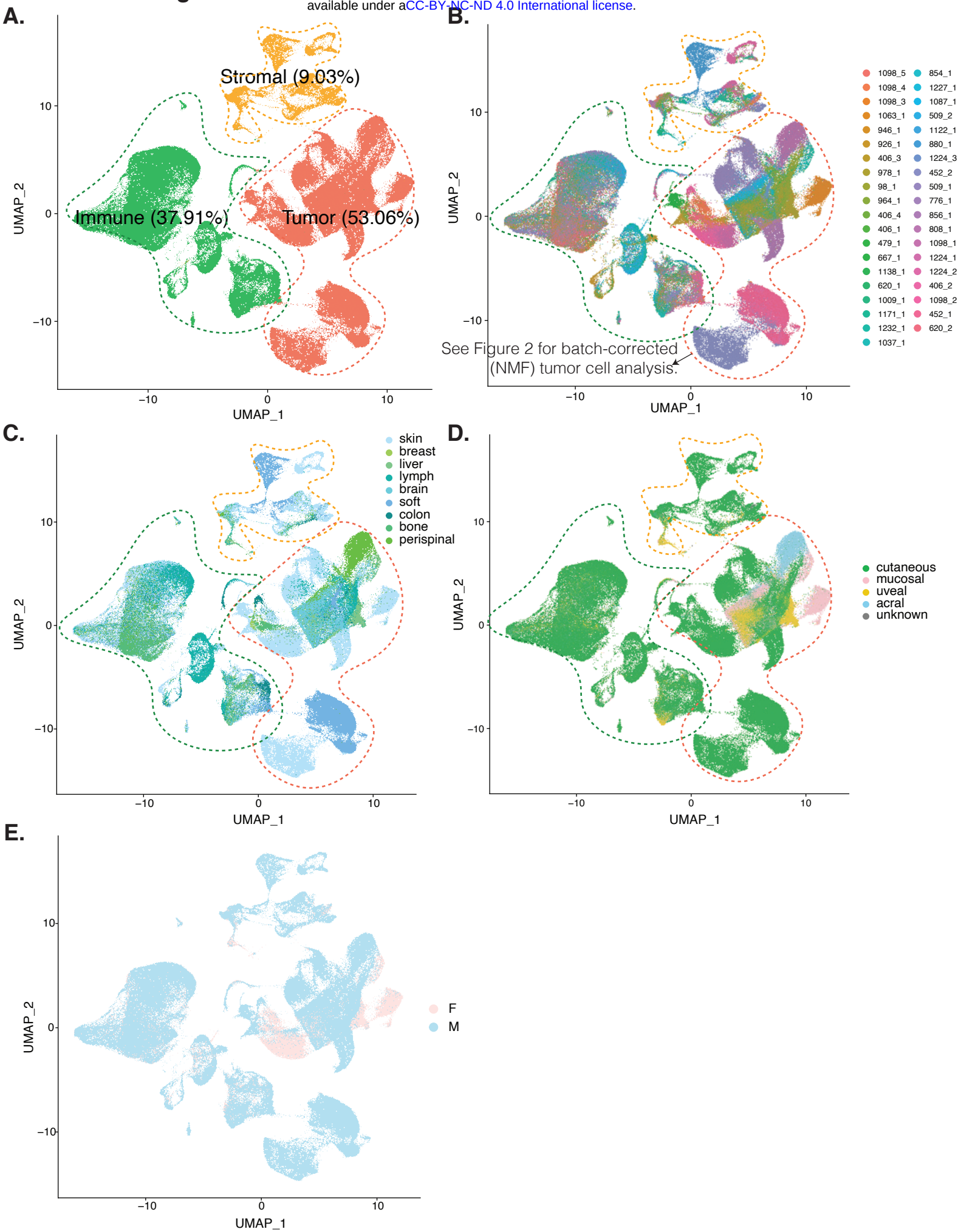

Extended Data Figure 2.

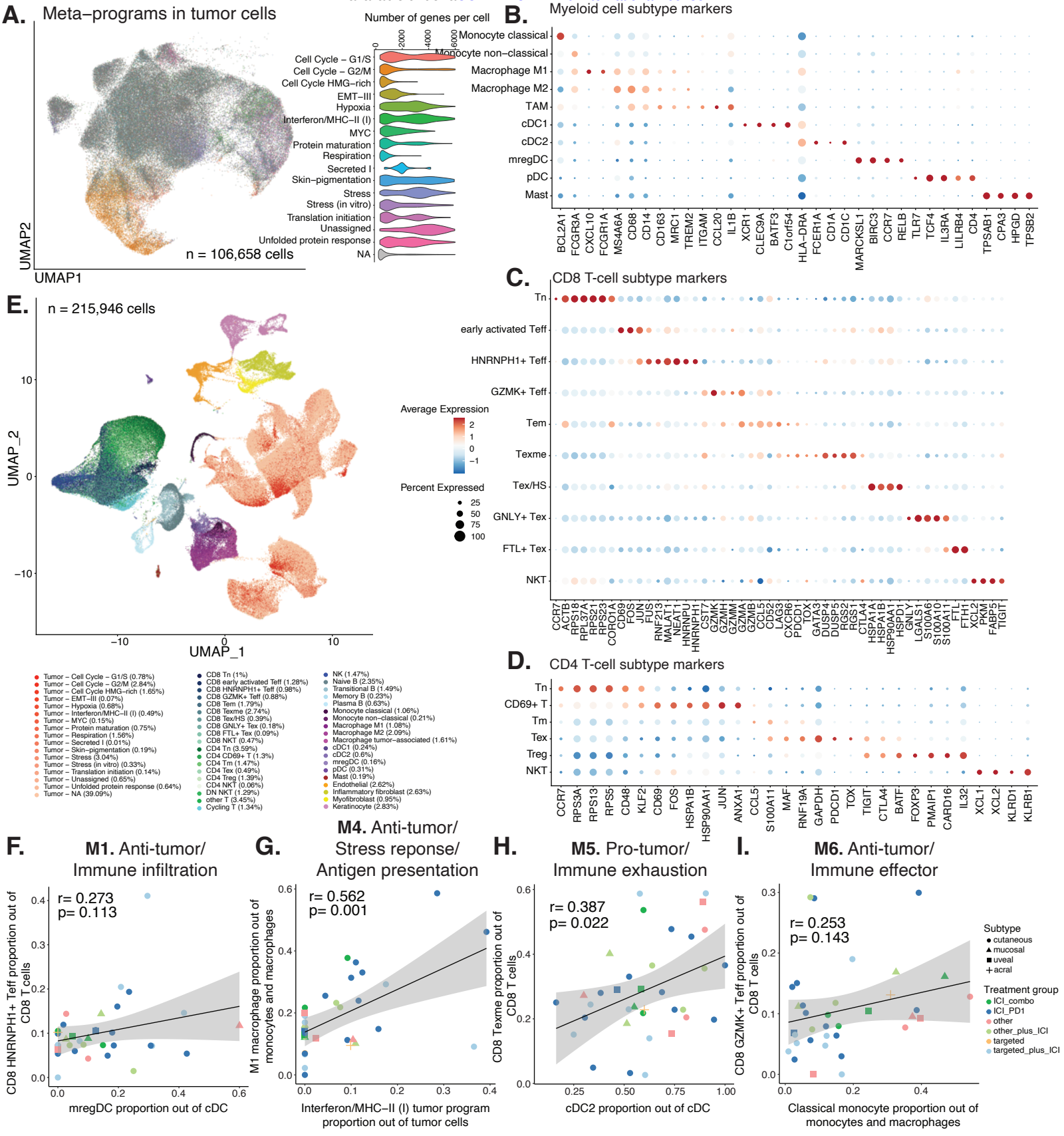

Extended Data Figure 3.

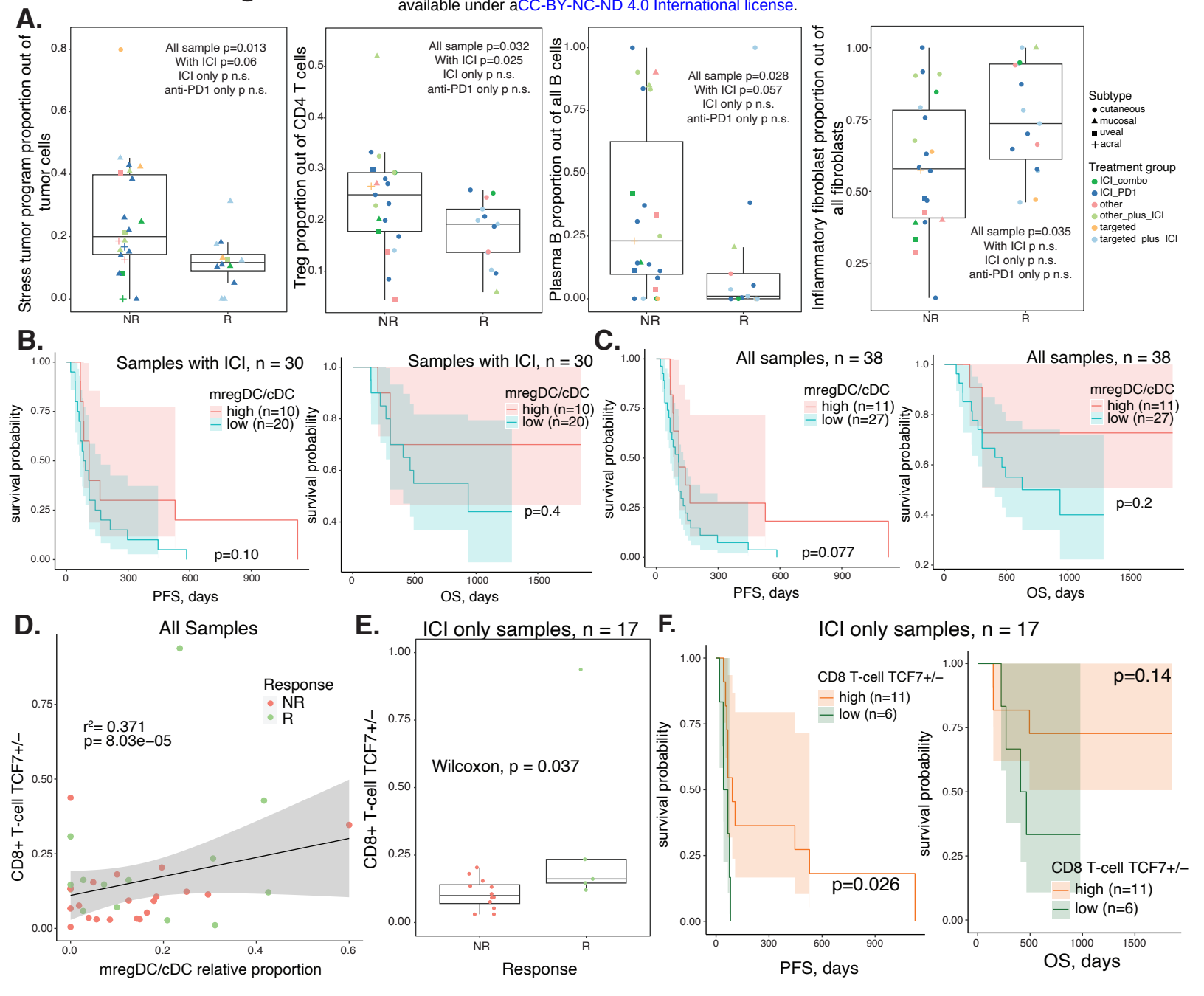

Extended Figure 4

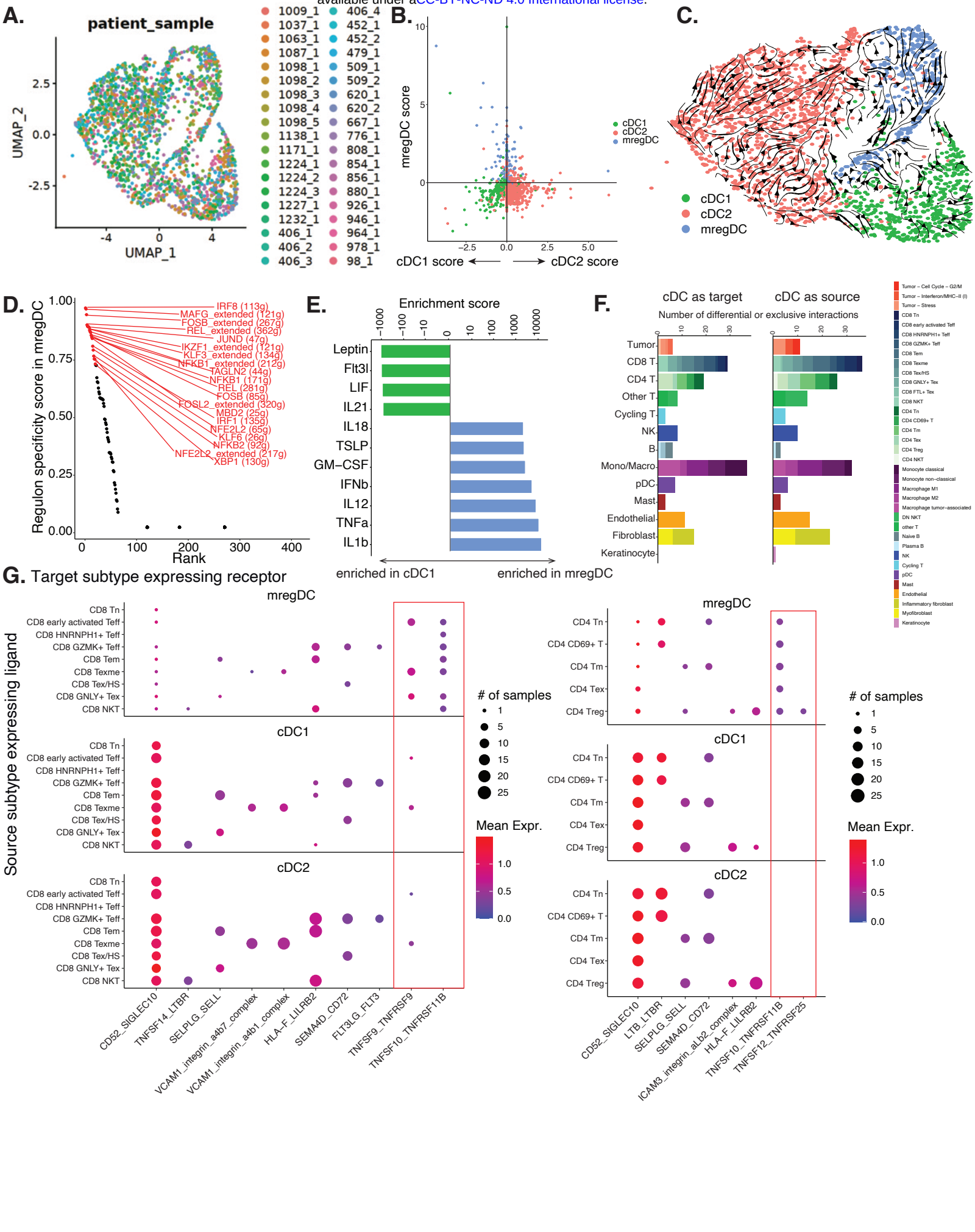

Extended Figure 5.

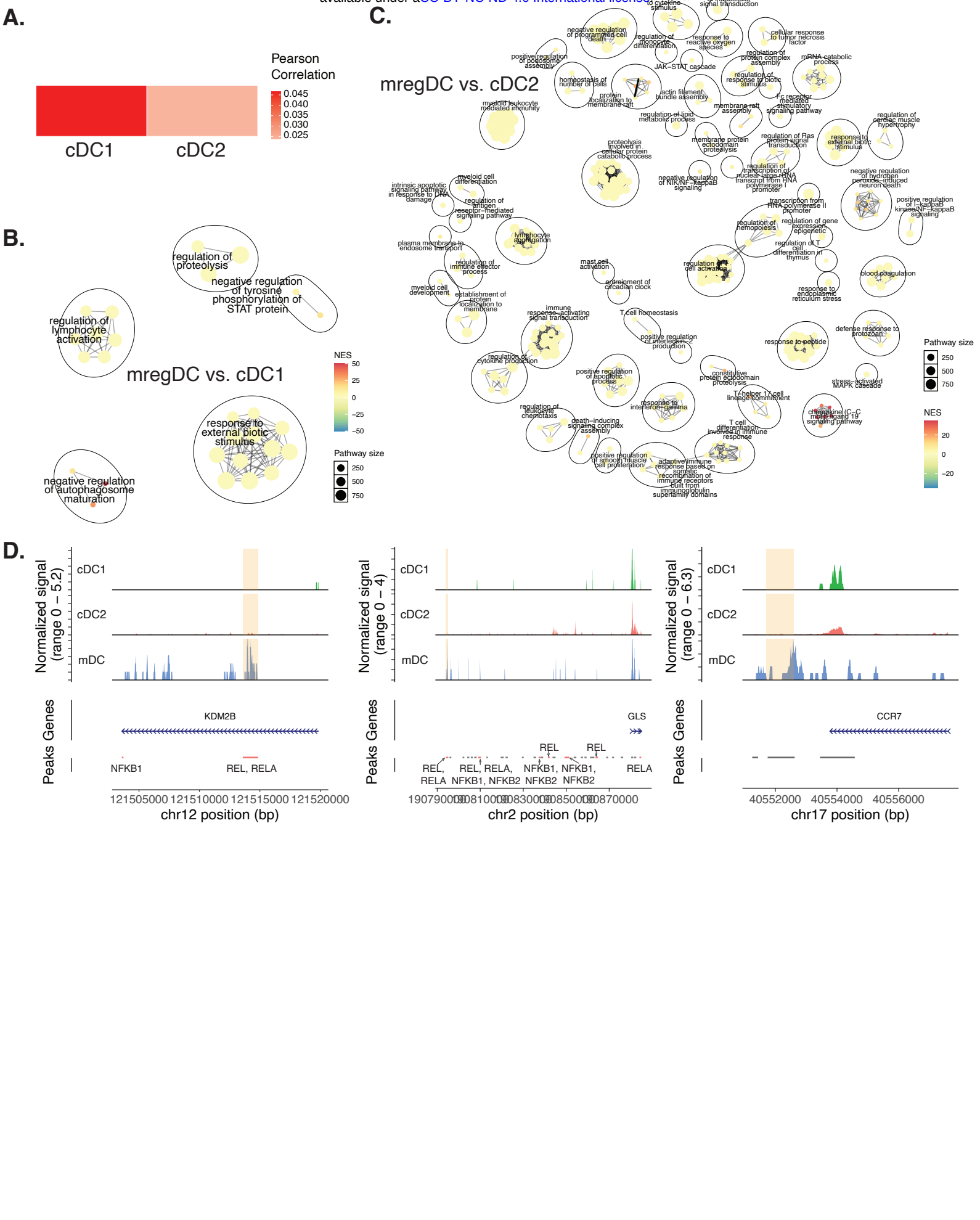

Extended Figure 6

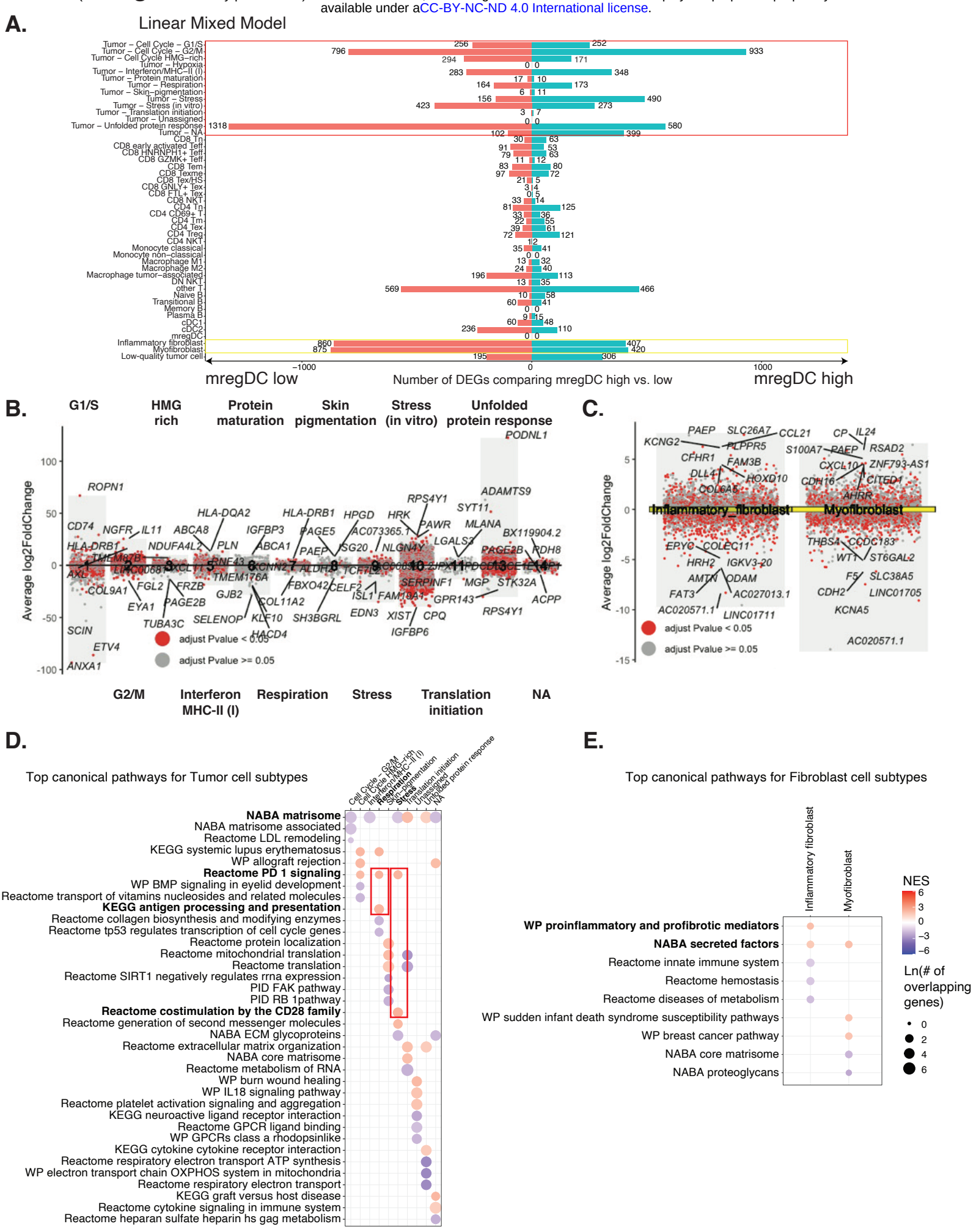

Supplementary Figure 1

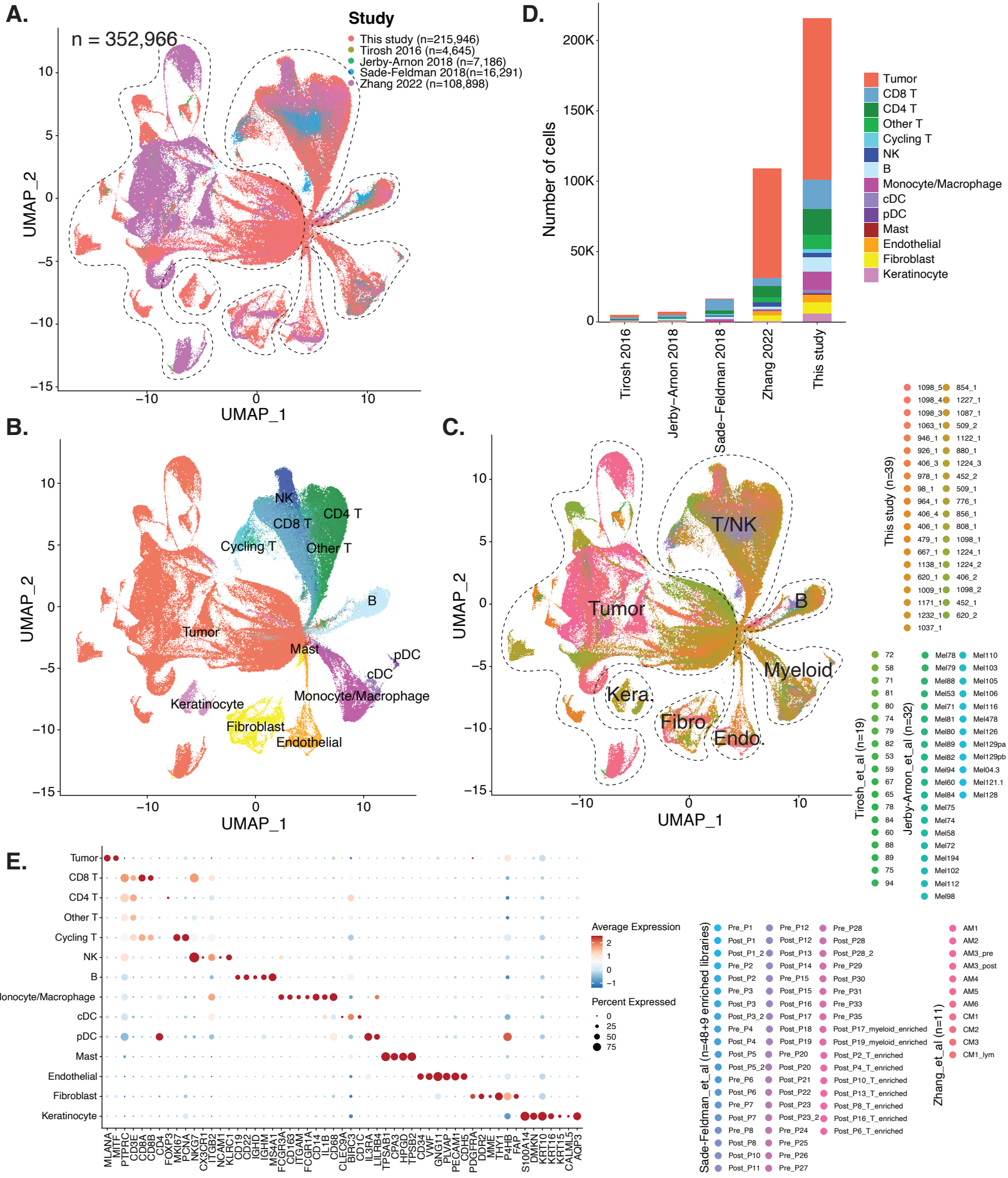

Reference:
1.Tirosh, I. et al. Dissecting the multicellular ecosystem of metastatic melanoma by single-cell RNA-seq. Science 352, 189–196 (2016).
2.Jerby-Arnon, L. et al. A Cancer Cell Program Promotes T Cell Exclusion and Resistance to Checkpoint Blockade. Cell 175, 984–997.e24 (2018).
3.Sade-Feldman, M. et al. Defining T Cell States Associated with Response to Checkpoint Immunotherapy in Melanoma. Cell 175, 998–1013.e20 (2018).
4.Zhang, C. et al. A single-cell analysis reveals tumor heterogeneity and immune environment of acral melanoma. Nat. Commun. 13, 7250 (2022).

Supplementary Figure 2.

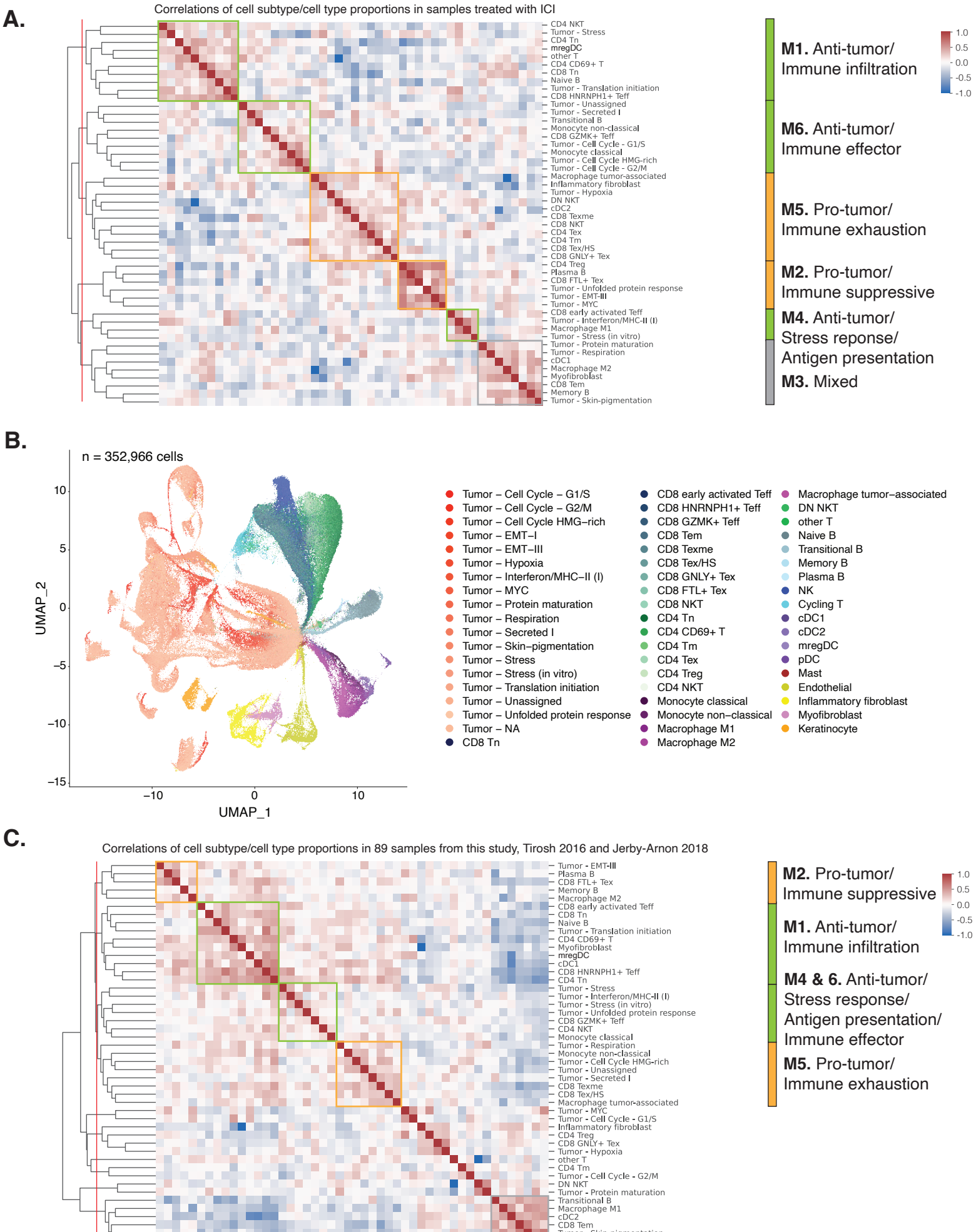

Supplementary Figure 3

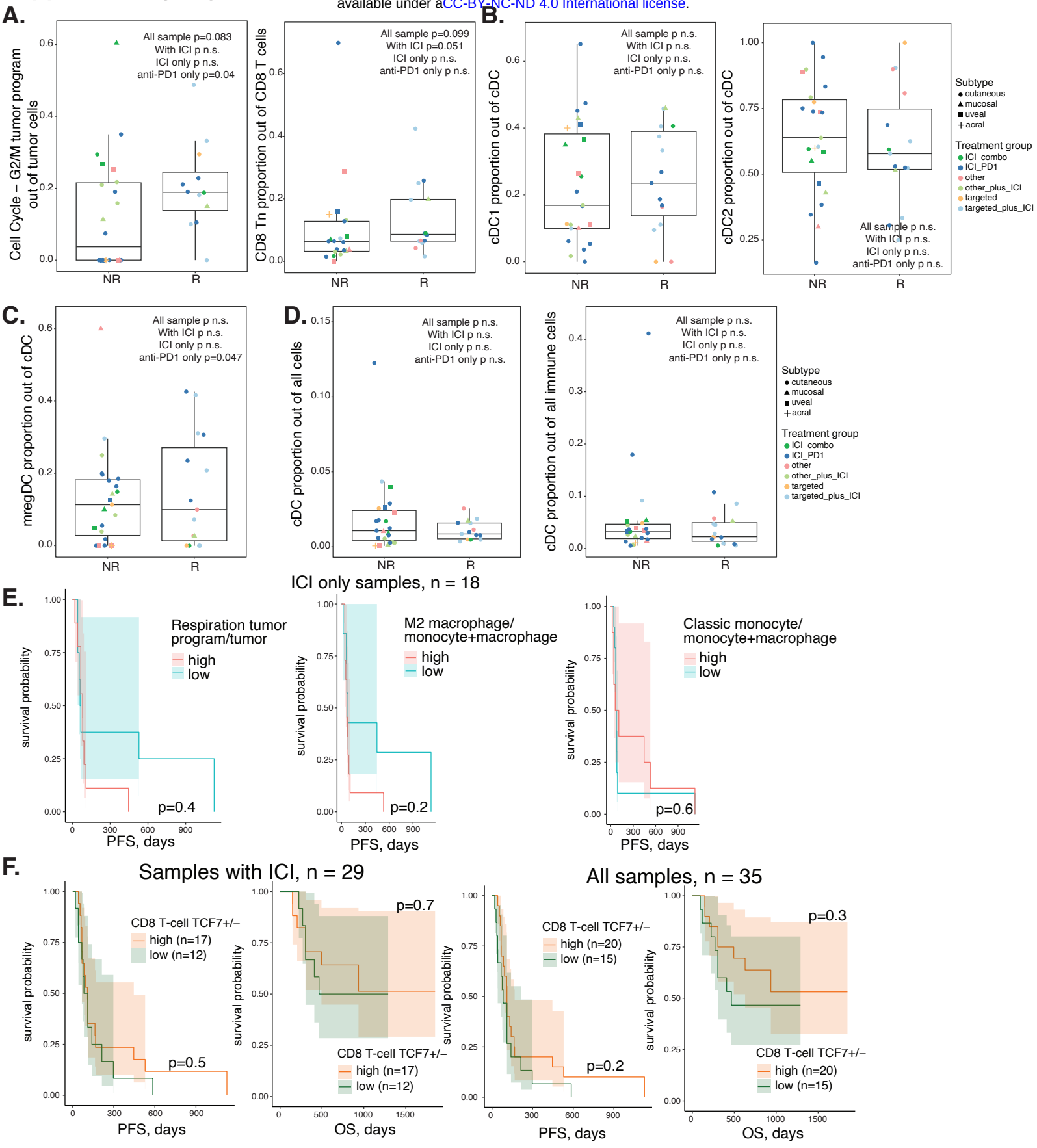

Supplementary Figure 4

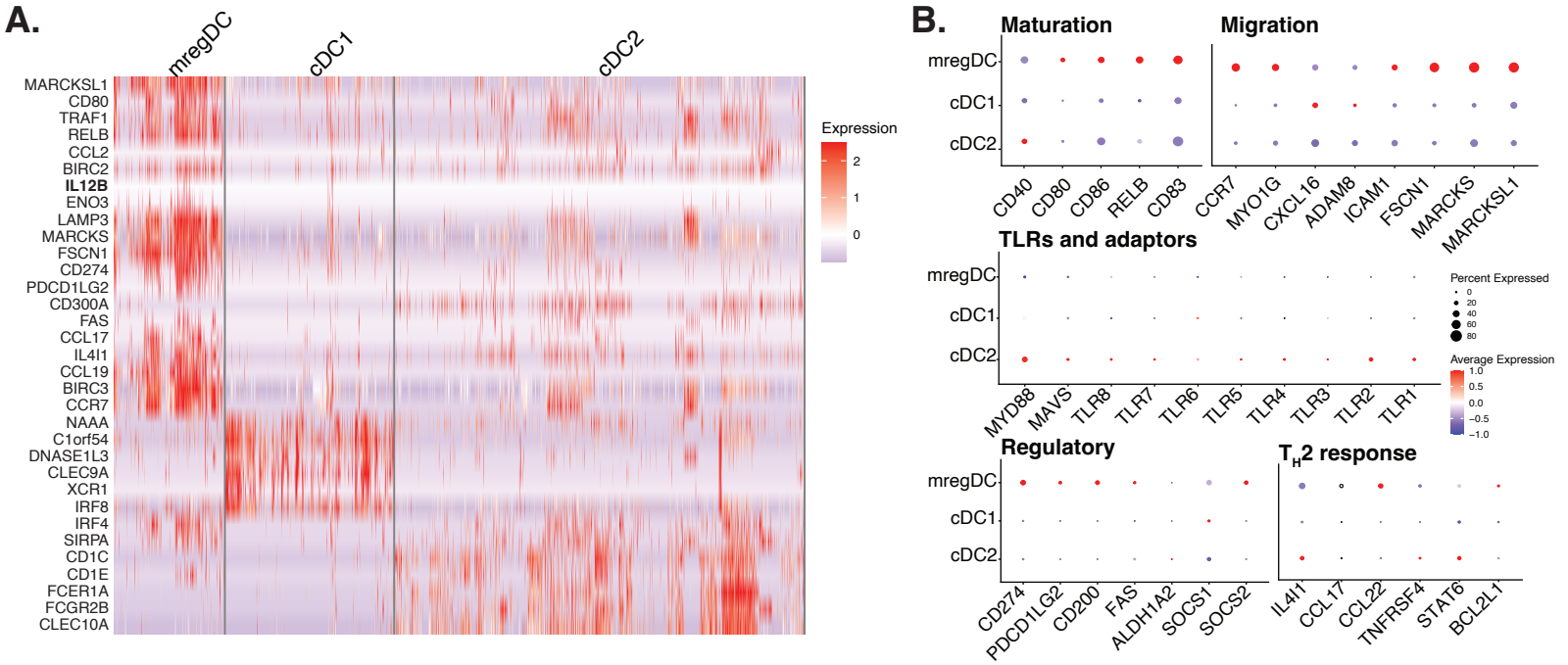

Maier, B. et al. A conserved dendritic-cell regulatory program limits antitumour immunity. Nature 580, 257–262 (2020).

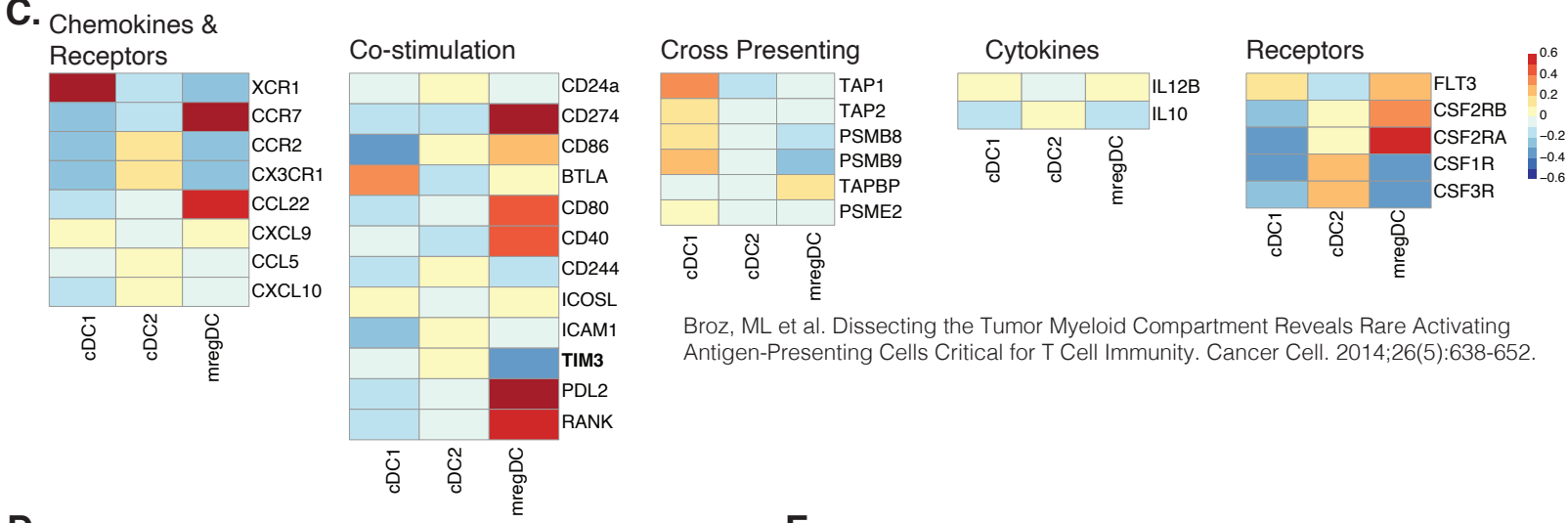

Broz, ML et al. Dissecting the Tumor Myeloid Compartment Reveals Rare Activating Antigen-Presenting Cells Critical for T Cell Immunity. Cancer Cell. 2014;26(5):638-652.

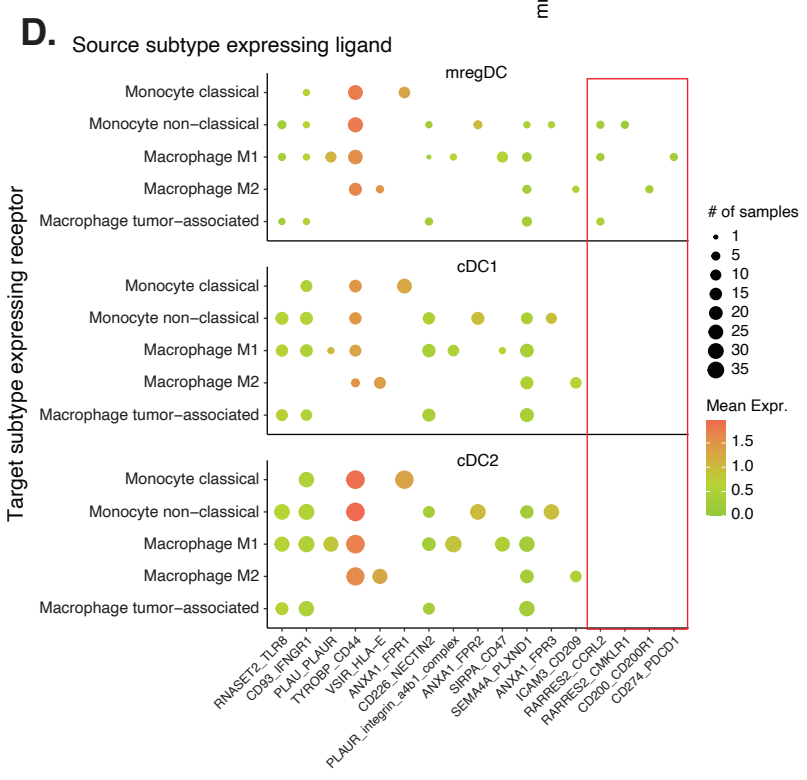

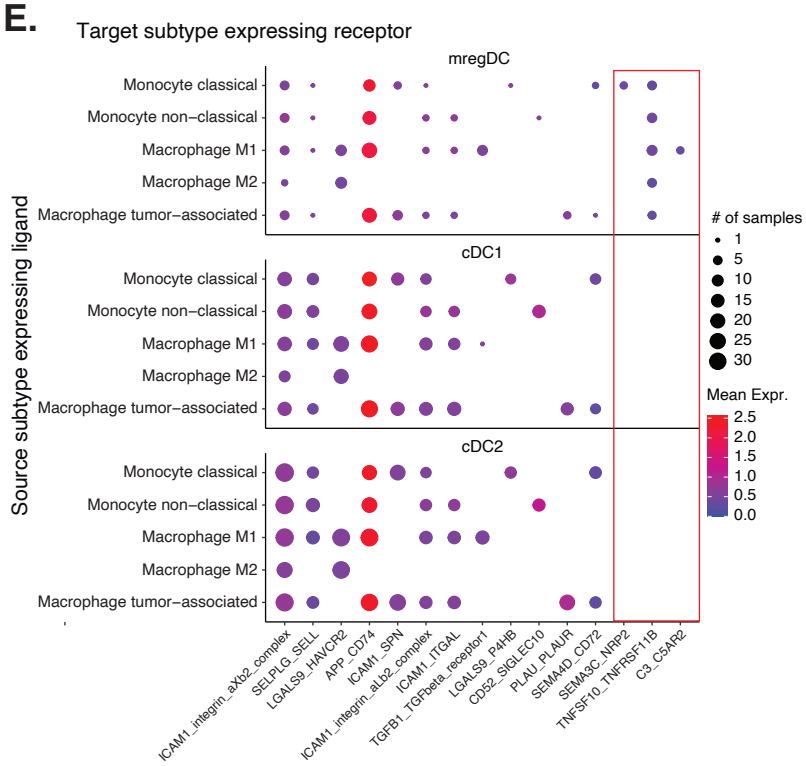

Supplementary Figure 5.